CM^2 Magazine

第 132 期

南方科技大学海洋磁学中心主编

https://cm2.sustech.edu.cn/

创刊词

海洋是生命的摇篮，是文明的纽带。地球上最早的生命诞生于海洋，海洋里的生命最终进化成了人类，人类的文化融合又通过海洋得以实现。人因海而兴。

人类对海洋的探索从未停止。从远古时代美丽的神话传说，到麦哲伦的全球航行，再到现代对大洋的科学钻探计划，海洋逐渐从人类敬畏崇拜幻想的精神寄托演变成可以开发利用与科学研究的客观存在。其中，上个世纪与太空探索同步发展的大洋科学钻探计划将人类对海洋的认知推向了崭新的纬度：深海（deep sea）与深时（deep time）。大洋钻探计划让人类知道，奔流不息的大海之下，埋藏的却是亿万年的地球历史。它们记录了地球板块的运动，从而使板块构造学说得到证实；它们记录了地球环境的演变，从而让古海洋学方兴未艾。

在探索海洋的悠久历史中，从大航海时代的导航，到大洋钻探计划中不可或缺的磁性地层学，磁学发挥了不可替代的作用。这不是偶然，因为从微观到宏观，磁性是最基本的物理属性之一，可以说，万物皆有磁性。基于课题组的学科背景和对海洋的理解，我们对海洋的探索以磁学为主要手段，海洋磁学中心因此而生。

海洋磁学中心，简称 CM^2，一为其全名“Centre for Marine Magnetism”的缩写，另者恰与爱因斯坦著名的质能方程 $E = MC^2$ 对称，借以表达我们对科学巨匠的敬仰和对科学的不懈追求。

然而科学从来不是单打独斗的产物。我们以磁学为研究海洋的主攻利器，但绝不仅限于磁学。凡与磁学相关的领域均是我们关注的重点。为了跟踪反映国内外地球科学特别是与磁学有关的地球科学领域的最新研究进展，海洋磁学中心特地主办 CM^2 Magazine，以期与各位地球科学工作者相互交流学习、合作共进！

“海洋孕育了生命，联通了世界，促进了发展”。21 世纪是海洋科学的时代，由陆向海，让我们携手迈进中国海洋科学的黄金时代。

目 录

1. 高纬度调控全新世北美季风.....1
2. 麦斯里希特阶暖事件最晚期德干火山活动的 Hg 证据.....4
3. 在南大洋的大西洋部分，大气河流有助于夏季地表浮力强迫.....7
4. 晚渐新世南极冰量的气候与构造驱动因素.....11
5. 红海南部海底扩张、信风和降水之间的反馈关系.....14
6. 伊豆-小笠原弧前火山岩钻孔样品的古地磁和古纬度研究---对菲律宾海板块运动的启示.....16
7. 早维塞尔冰期基于石笋记录的欧洲西风带的漂移在 MIS 5a 期间存在百年尺度变化.....19
8. 保存完好的克拉通间岩石圈揭示澳大利亚的元古代拼合.....21
9. 上新世晚期南亚季风变化和北极海冰范围关系.....23
10. 北大西洋古新世-始新世极热期内外巨型磁化石的发现 25
11. 大陆溢流玄武岩驱动显生宙生物灭绝.....28
12. 气候网络曲率解释的不同厄尔尼诺类型遥相关模式.....30
13. 地中海东部末次间冰期十年际尺度海表温度变化.....32
14. 过去半个世纪全球海洋热量吸收的驱动力和分布.....34
15. 过去 230 kyr 亚北极太平洋环境生产力的高纬及低纬强迫 36
16. 理解 8.2 ka 冷事件和当前暖事件期间的全球季风降水变化.....39

1. 高纬度调控全新世北美季风

翻译人：仲义 zhongy@sustech.edu.cn

Routson, C.C., Erb, M.P., and McKay, N.P., ***High latitude modulation of the Holocene North American Monsoon*** *[J] Geophysical Research Letters, 2022, 49(16), e2022GL099772.*

https://doi.org/10.1029/2022GL099772

摘要：北美季风是墨西哥和美国西北部主要的降水来源。西风带可以一直季风环流和影响季风形成时间、强度和范围。最近北极变暖正在不断降低极地与赤道地区的温度梯度，进而减弱西风带；然而，关于北美季风的变化意义仍然不清楚。本文作者展示了一个全新世北美季风强度指数。作者发现季风强度在 7000 年前达到顶峰，此后逐渐减弱。温度、水文和上升流指标以及气候模型都显示北美季风在全新世时期受到西风带的调控作用。如果观测的全新世模式按照全球变暖的发展下去，未来经向温度梯度和西风带减弱会导致北美季风更强。

ABSTRACT: The North American monsoon (NAM) is an important source of rainfall to much of Mexico and southwestern United States. Westerly winds (westerlies) can suppress monsoon circulation and impact monsoon timing, intensity, and extent. Recent Arctic warming is reducing the temperature gradient between the equator and the pole, which could weaken the westerlies; however, the implications of these changes on the NAM are uncertain. Here we present a new composite index of the Holocene NAM. We find monsoon strength reached a maximum circa 7,000 years ago and has weakened since then. Proxy observations of temperature, hydroclimate and upwelling, along with model simulations, show that the NAM was modulated by the westerlies over the Holocene. If the observed Holocene pattern holds for current warming, a weaker meridional temperature gradient and weaker westerlies could lead to a stronger future NAM.

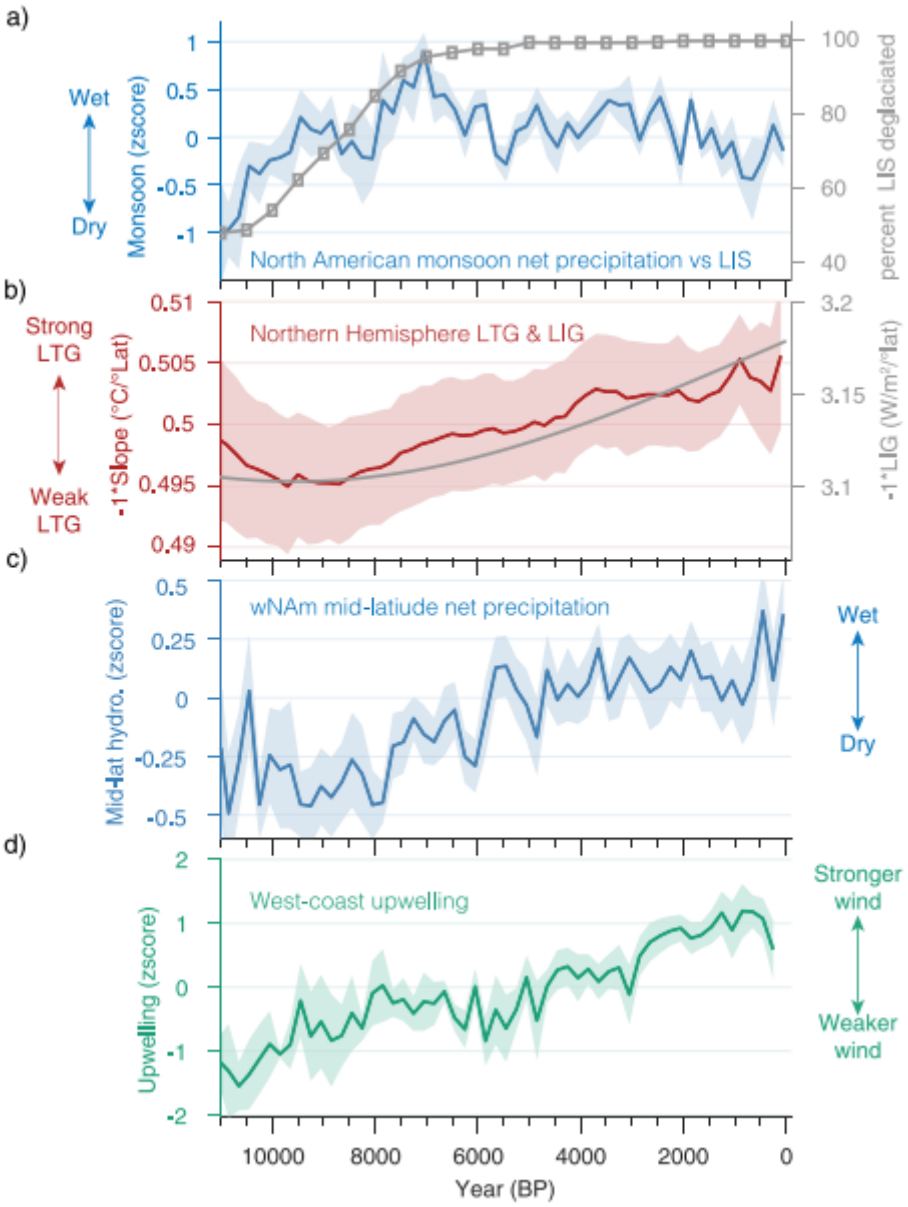

Figure 1. Holocene climates of the North American monsoon (NAM). (a) The Holocene NAM composite index (blue) with the percent area of the Laurentide Ice Sheet deglaciated compared to its Local Last Glacial Maximum calculated from the ICE-7G glacial model results (gray) (Peltier et al., 2015). (b) The Northern Hemisphere latitudinal temperature gradient (red) with the Northern Hemisphere latitudinal insolation gradient (LIG) (gray). The calculated axes have been inverted so a stronger Latitudinal Temperature Gradient and LIG are up (c) The western North American mid-latitude net precipitation composite index (blue). (d) West coast upwelling composite index as an indicator of westerly wind-strength (green). The shading represents ±1 standard deviation uncertainties of a sample-with-replacement estimation of the mean over bootstrap 500 iterations.

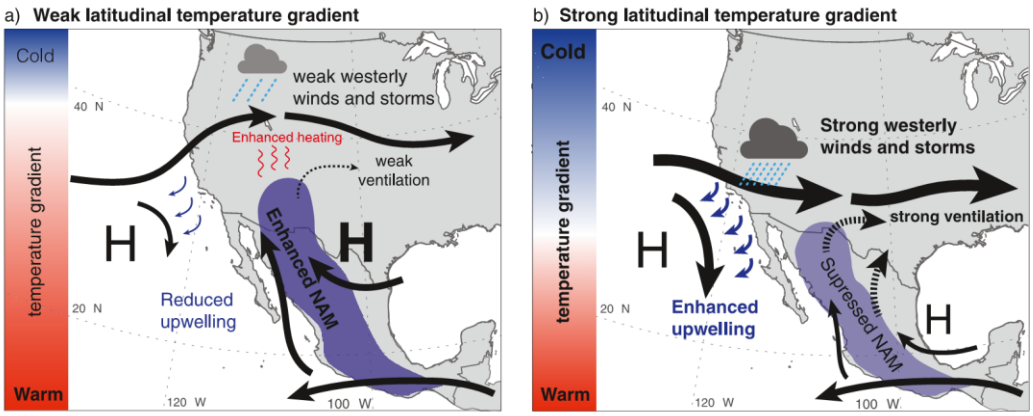

Figure 2. Conceptual diagram showing circulation change with (a) weak and (b) strong Latitudinal Temperature Gradient (LTG). Winds (solid black arrows), the LTG (red-to-blue gradient), Pacific and Bermuda high pressure systems (H), coastal upwelling (blue arrows), and ventilation of the North American monsoon (NAM) (dashed black arrows) are illustrated. (a) A weak LTG leads to weaker westerly winds, reduced westerly storm systems, reduced coastal upwelling, a northward shift in the Pacific High, and enhanced NAM. (b) A strong LTG leads to enhanced westerly storm-track sourced rainfall, enhanced coastal upwelling, a southward shifted Pacific High, increased ventilation, and a suppressed NAM.

2. 麦斯里希特阶暖事件最晚期德干火山活动的 Hg 证据

翻译人：蒋晓东 jiangxd@sustech.edu.cn

Li S, Grasby S E, Zhao X D, et al. ***Mercury evidence of Deccan volcanism driving the Latest Maastrichtian warming event*** *[J]. Geology, (2022). 50, 1140-1146.*
https://doi.org/10.1130/G50016.1

摘要：德干大火山岩省的喷发事件和生态响应一直存在争议。海洋沉积物中广泛的记录了德干火山活动对白垩-第三系交界时期的影响，而对陆地影响的直接证据仍然缺少。我们使用了 Hg 含量和同位素组成作为火山活动的指标，来评估火山活动对陆地环境的响应。我们选取了中国东部穿过 KPg 界面的两个钻孔进行研究，这两个孔记录了不同的沉积环境：胶莱盆地的碎屑沉积和平邑盆地的碳酸盐沉积。两个孔在 KPg 界面之前都具有较高的 Hg 含量。胶莱盆地中几乎一致的非质量分馏的 Hg 同位素指示 KPg 边界下火山源的 Hg 峰值。平邑盆地中的 Hg 同位素同样指示了火山源的 Hg 来源，但在其峰值前和后具有低 Δ^{199}Hg 值的陆源信号。Hg 富集的程度在地层学中与麦斯里希特阶暖事件的开始具有很好的对应关系，并且与有机碳同位素和碳酸盐同位素负漂一致。这表明此时全球碳循环的扰动是由德干火山活动引起。在 KPg 边界前德干火山活动的陆地记录为德干大火山岩省在麦斯里希特阶暖事件最晚期的全球影响提供了强有力的证据。

ABSTRACT: The timing and ecological impacts of the Deccan Traps large igneous province eruption are vigorously debated. Pre–Cretaceous-Paleogene (KPg) boundary impacts of Deccan volcanism have been widely identified in marine sediments, but direct evidence of terrestrial impacts remains rare. We used mercury concentrations and isotopic compositions, a proxy for volcanic activity, to assess impacts on terrestrial environments. We studied two drill cores across the KPg boundary in eastern China that represent two different depositional environments: clastic deposits in the Jiaolai Basin and carbonate deposits in the Pingyi Basin. Both drill cores exhibit strong Hg enrichment prior to the KPg boundary. Near consistent mass-independent fractionation (MIF) of odd-Hg isotopes (odd-MIF) in the Jiaolai Basin likely indicates a volcanogenic source of Hg spikes below the KPg boundary. Odd-MIF isotopes in the Pingyi Basin likewise suggest a

volcanogenic Hg source but with a terrestrial Hg signature of lower Δ^{199}Hg values before and after the Hg spike interval. The Hg enrichment level can be stratigraphically correlated to the beginning of the Latest Maastrichtian warming event (LMWE) and is consistent with a strong, negative carbon-isotope excursion (CIE) in both $\delta^{13}C_{org}$ (organic matter) and $\delta^{13}C_{carb}$ (carbonate), suggesting a disturbance of the global carbon cycle induced by a major pulse of Deccan Traps volcanism. Our discovery of a terrestrial record of pre-KPg boundary Deccan volcanism provides robust evidence of global influence of the Deccan Traps large igneous province during the LMWE.

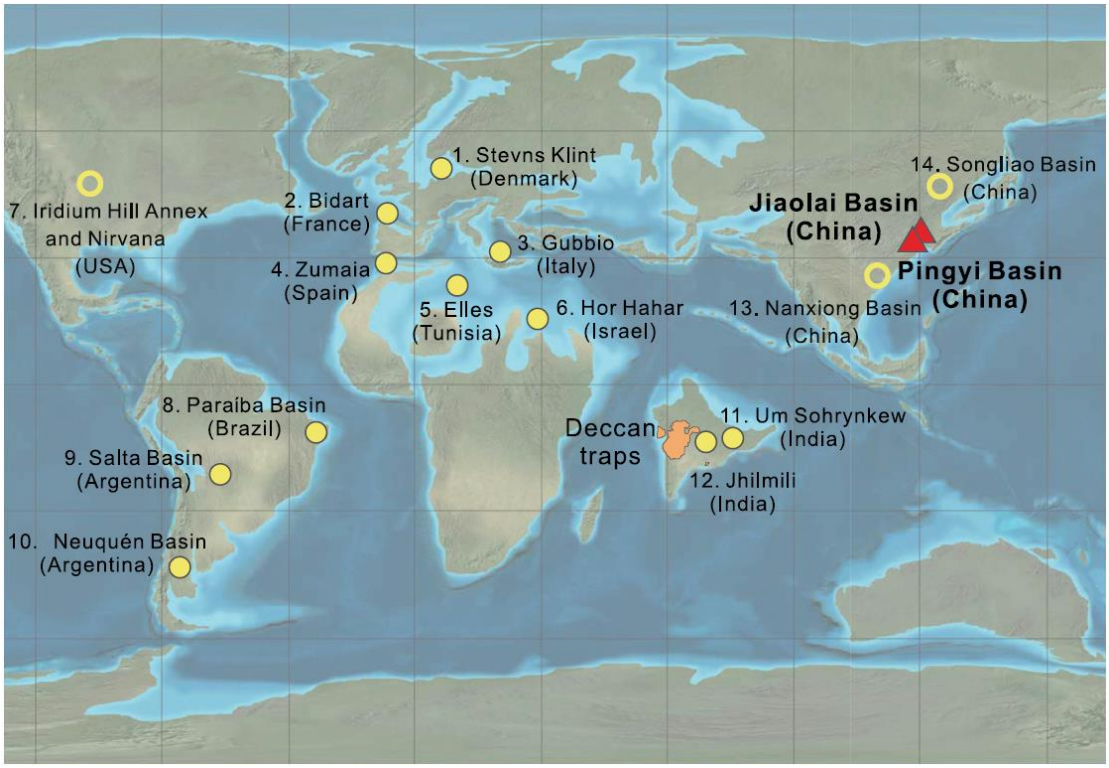

Figure 1. Paleogeographic map showing locations of the cores studied (red triangles) and the Deccan Traps (orange area). Locations of Cretaceous-Paleogene (KPg) sections where Hg anomalies have been documented are indicated by solid yellow circles for marine sections and open yellow circles for terrestrial sections (Sial et al., 2013, 2016; Font et al., 2016, 2018; Fendley et al., 2019; Keller et al., 2020; Zhao et al., 2021; Gu et al., 2022). The global paleogeography Mollweide projection base map of the KPg boundary is used with permission from the license holder ©2016 Colorado Plateau Geosystems, Inc.

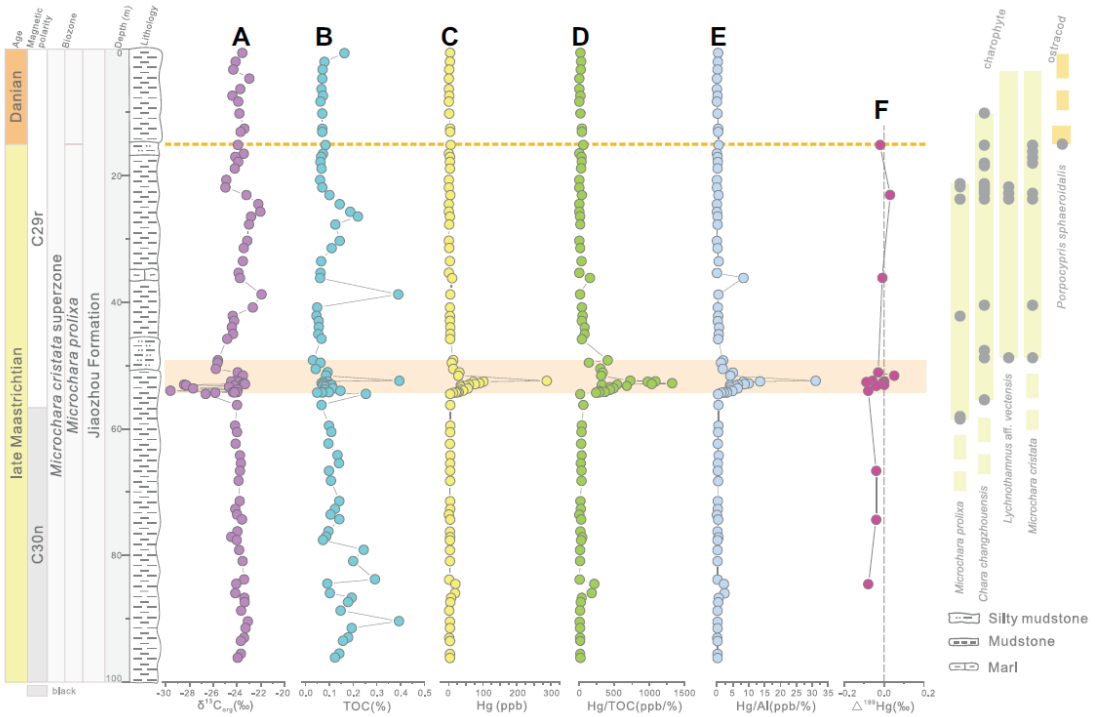

Figure 2. Mercury concentrations and organic carbon isotopic compositions in boreholes in the Jiaolai Basin (eastern China): (A) δ^{13}Corg; (B) total organic carbon (TOC); (C) Hg; (D) Hg/TOC; (E) Hg/Al; and (F) Δ^{199}Hg. The horizontal rectangle represents the Hg spike interval, and the dotted orange line marks the potential KPg boundary. The gray circles represent samples with charophytes and ostracods, and the yellow/orange bars represent the distribution of charophytes/ostracods species.

3. 在南大洋的大西洋部分，大气河流有助于夏季地表浮力强迫

翻译人：盖聪聪 gaicc@sustech.edu.cn

Edholm J M, Swart S, Plessis M D, & Nicholson S-A. ***Atmospheric rivers contribute to summer surface buoyancy forcing in the Atlantic sector of the Southern Ocean*** *[J]. Geophysical Research Letters, 2022, 49, e2022GL100149.*
https://doi.org/10.1029/2022GL100149

摘要：大气河流（ARs）在全球范围内主导水分输送；然而，目前尚不清楚 AR 对海面浮力的影响。本研究利用 2018 年 12 月 19 日至 2019 年 2 月 12 日（55 天）期间在亚极地南大洋（54° S，0° E）部署的波浪滑翔机高分辨率表面观测结果来探索 AR 获得的表面浮力。当 AR 伴随风暴时，相关的降水显著增强（189%）。此外，AR 产生的降水的日累积为海表海洋提供了浮力增益，相当于地表热通量造成的变暖。在 55 天里，总降水量的 47%是由 AR 带来的，这相当于夏季海表海洋浮力增加了 10%。本研究表明，ARs 在亚极地南大洋夏季降水中发挥着重要作用，并且它们可以改变从天气到季节时间尺度的上层海洋浮力收支。

ABSTRACT: Atmospheric rivers (ARs) dominate moisture transport globally; however, it is unknown what impact ARs have on surface ocean buoyancy. This study explores the surface buoyancy gained by ARs using high-resolution surface observations from a Wave Glider deployed in the subpolar Southern Ocean (54°S, 0°E) between 19 December 2018 and 12 February 2019 (55 days). When ARs combine with storms, the associated precipitation is significantly enhanced (189%). In addition, the daily accumulation of AR-induced precipitation provides a buoyancy gain to the surface ocean equivalent to warming by surface heat fluxes. Over the 55 days, ARs accounted for 47% of the total precipitation equating to 10% of the summer surface ocean buoyancy gain. This study indicates that ARs play an important role in the summer precipitation over the subpolar Southern Ocean and that they can alter the upper-ocean buoyancy budget from synoptic to seasonal timescales.

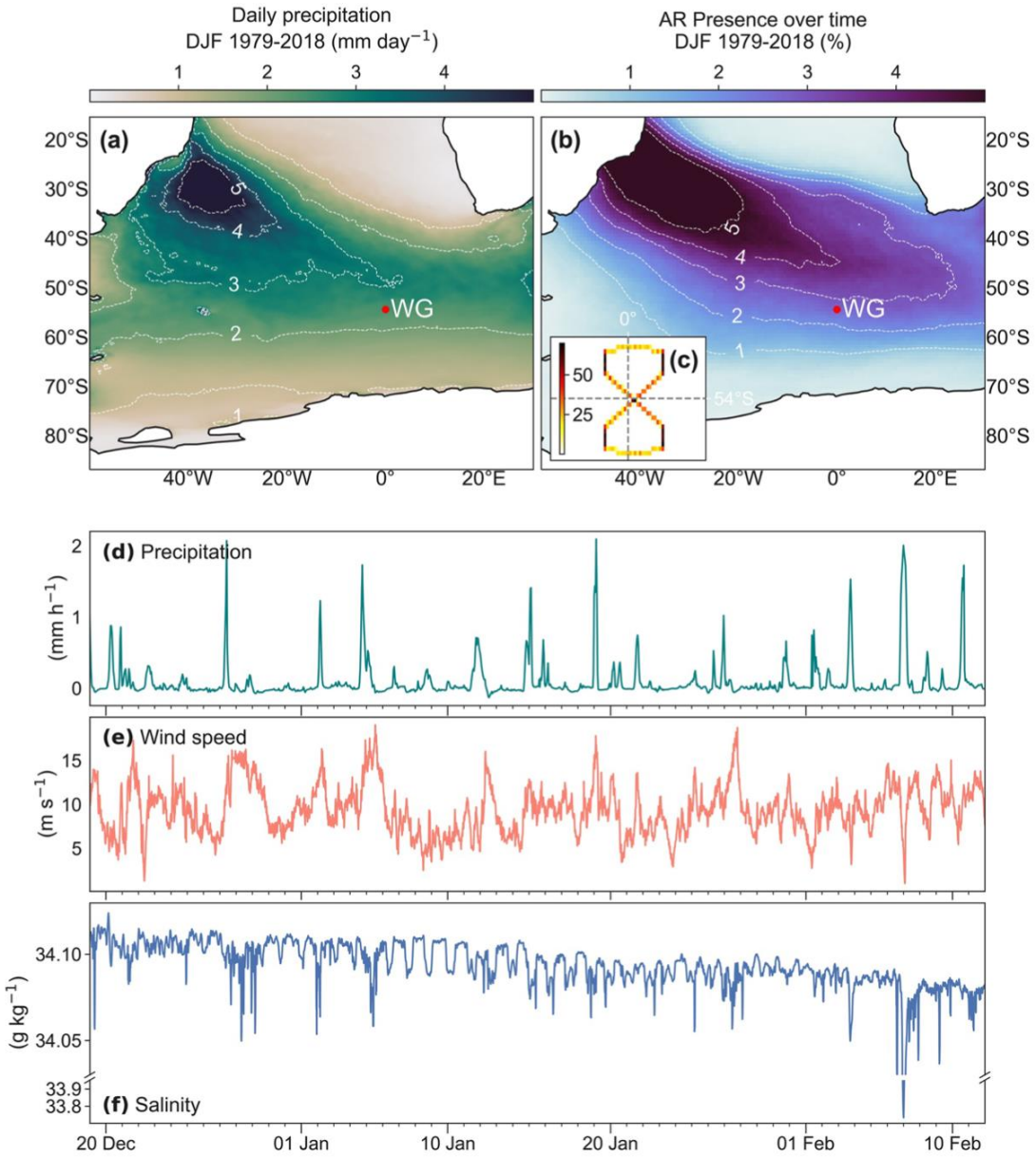

Figure 1. (a) Austral summer climatology (DJF, 1979–2018) of (a) daily precipitation and (b) atmospheric river distribution in time and space, derived from ERA5. The location of the Wave Glider (WG) deployment is marked in both (a and b). (c) Distribution (heat map) of the WG sampling pattern (n = 3,960). (d) ERA5 hourly precipitation (P − E) at the location of the WG. Time series (dt = 20 min) of near-surface (0.5 m) wind speed (e) and absolute salinity (f) measured at the surface (0.3 m depth) by the WG during austral summer in 2018–2019. Note the break in the y axis for the salinity magnitude.

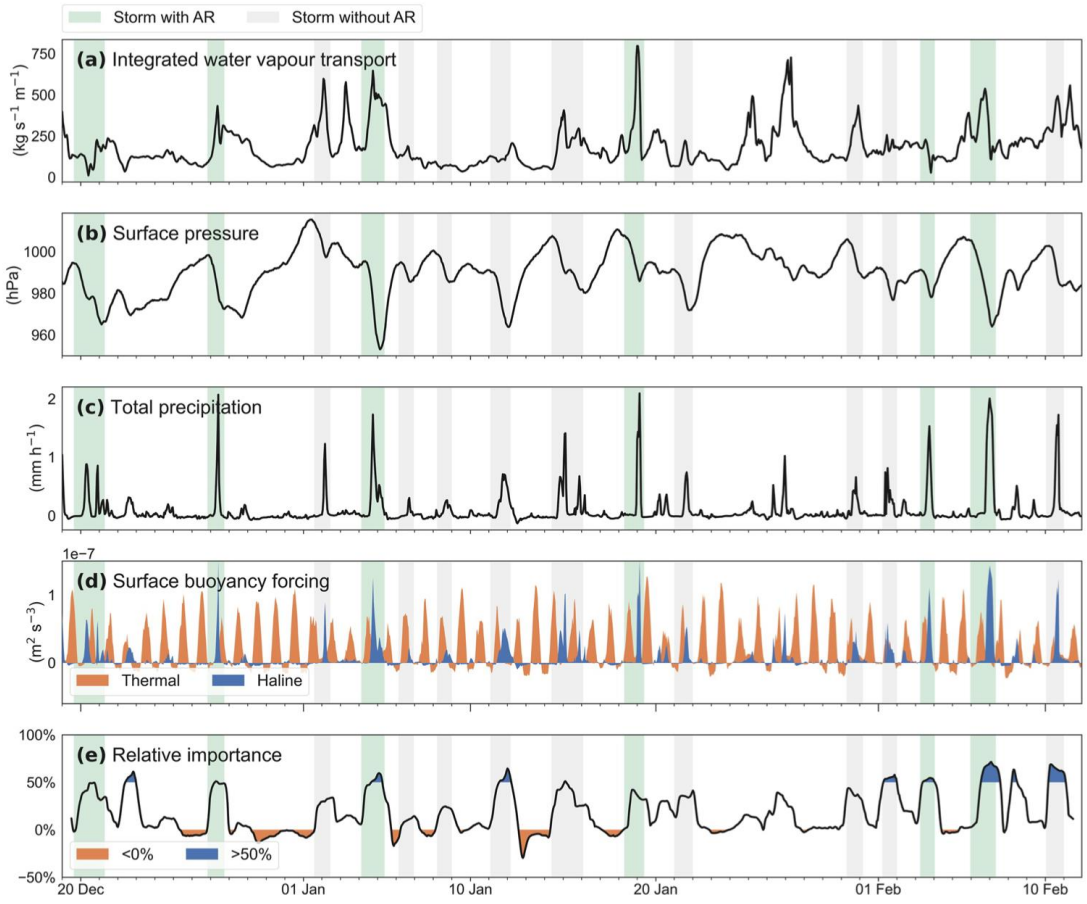

Figure 2. Integrated Water Vapor Transport (a), sea level pressure (b), and total precipitation (c) from ERA5 collocated in space and time to Wave Glider (WG) observations. (d) Thermal and haline components of surface buoyancy forcing derived from ERA5 and observations by the WG. (e) The relative contribution of the haline component to the total surface buoyancy forcing (in percent). Periods when the haline component contributed more than 50% or less than 0% are shaded. These negative percentages indicate periods of evaporation. Vertical bands in all panels highlight the period of a passing storm, and the color determines if an atmospheric river was present (green) or not (gray) during the storm.

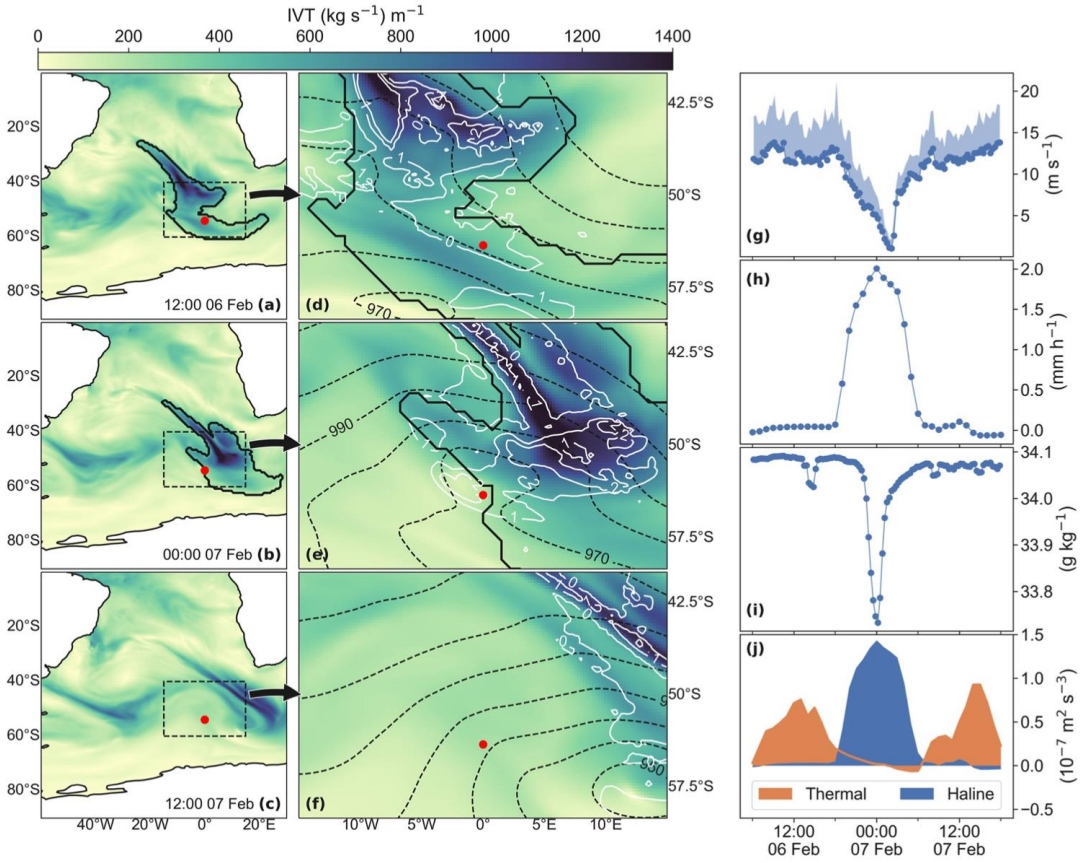

Figure 3. A case study illustrating the surface ocean response to an atmospheric river-linked precipitation event (7 February 2019) as measured by the Wave Glider (WG). (a–f) Snapshots of Integrated Water Vapor Transport (IVT), derived from ERA5 data at three different times: at maximum precipitation for the event and 12 hr before and after. An atmospheric river is marked by black contours in (a, b) and (d, e). (a–c) Large-scale context and spatial extent of IVT over the Atlantic sector of the Southern Ocean. The equivalent "zoomed-in" panels (d–f) are marked with the black-dashed box and the red dot is the WG site in both sets of maps. In (d–f), isobars (dashed black) and isohyets (precipitation, solid white) are added. (g) In situ wind speed and 20-min maximum gusts (m s−1) as measured by the WG, (h) ERA5 precipitation at the WG site, and (i) in situ surface salinity observed by the WG. (j) Haline and thermal contribution to surface buoyancy. The dots in (g–i) represent the temporal resolution, 20 min for the WG data, and hourly for the ERA5 data.

4. 晚渐新世南极冰量的气候与构造驱动因素

翻译人：张琪 zhangq7@sustech.edu.cn

Duncan B, McKay R, Levy R, et al, ***Climatic and tectonic drivers of late Oligocene Antarctic ice volume*** *[J]. Nature Geoscience, 2022.*
https://doi.org/10.1038/s41561-022-01025-x

摘要：南极冰盖的新生代演化被认为主要是由辐射强迫的长期变化驱动的，但南极的构造演化可能也发挥了实质性的作用。虽然深海有孔虫氧同位素记录提供了全球大陆冰量和海洋温度的综合测量方法，但却无法提供对南极冰盖动态的非辐射影响的直接见解。本文中，作者提供一份南极罗斯海和近海威尔克斯陆地新生代上层海洋温度汇总，由古菌的膜脂分布生成。 作者发现海洋温度、大气二氧化碳和氧同位素的变化趋势很大程度上是同步的。当高纬度开始冷却，尽管来自氧同位素的解释表明全球变暖和冰量损失，然而，上述同步变化趋势在渐新世晚期却并不明确。作者认为，南极西部冰盖的退缩是由构造驱动的海洋海侵引起的，温暖的地表水阻止了海洋冰盖的增长。只有在渐新世-中新世过渡时期海洋温度进一步降低，轨道条件寒冷，大气二氧化碳含量低的情况下，海洋冰盖才会扩张。本文的研究结果支持对大气二氧化碳的阈值响应，低于这个阈值南极洲冰盖生长，高于这个阈值海洋变暖加剧了它们的消退。

ABSTRACT: Cenozoic evolution of the Antarctic ice sheets is thought to be driven primarily by long-term changes in radiative forcing, but the tectonic evolution of Antarctica may also have played a substantive role. While deep-sea foraminiferal oxygen isotope records provide a combined measure of global continental ice volume and ocean temperature, they do not provide direct insights into non-radiative influences on Antarctic Ice Sheet dynamics. Here we present an Antarctic compilation of Cenozoic upper-ocean temperature for the Ross Sea and offshore Wilkes Land, generated by membrane lipid distributions from archaea. We find trends of ocean temperature, atmospheric carbon dioxide and oxygen isotopes largely co-vary. However, this relationship is less clear for the late Oligocene, when high-latitude cooling occurred despite interpretation of oxygen isotopes suggesting global warming and ice-volume loss. We propose this retreat of the West

Antarctic Ice Sheet occurred in response to a tectonically driven marine transgression, with warm surface waters precluding marine-based ice-sheet growth. Marine ice-sheet expansion occurred only when ocean temperatures further cooled during the Oligocene–Miocene transition, with cold orbital conditions and low atmospheric carbon dioxide. Our results support a threshold response to atmospheric carbon dioxide, below which Antarctica's marine ice sheets grow, and above which ocean warming exacerbates their retreat.

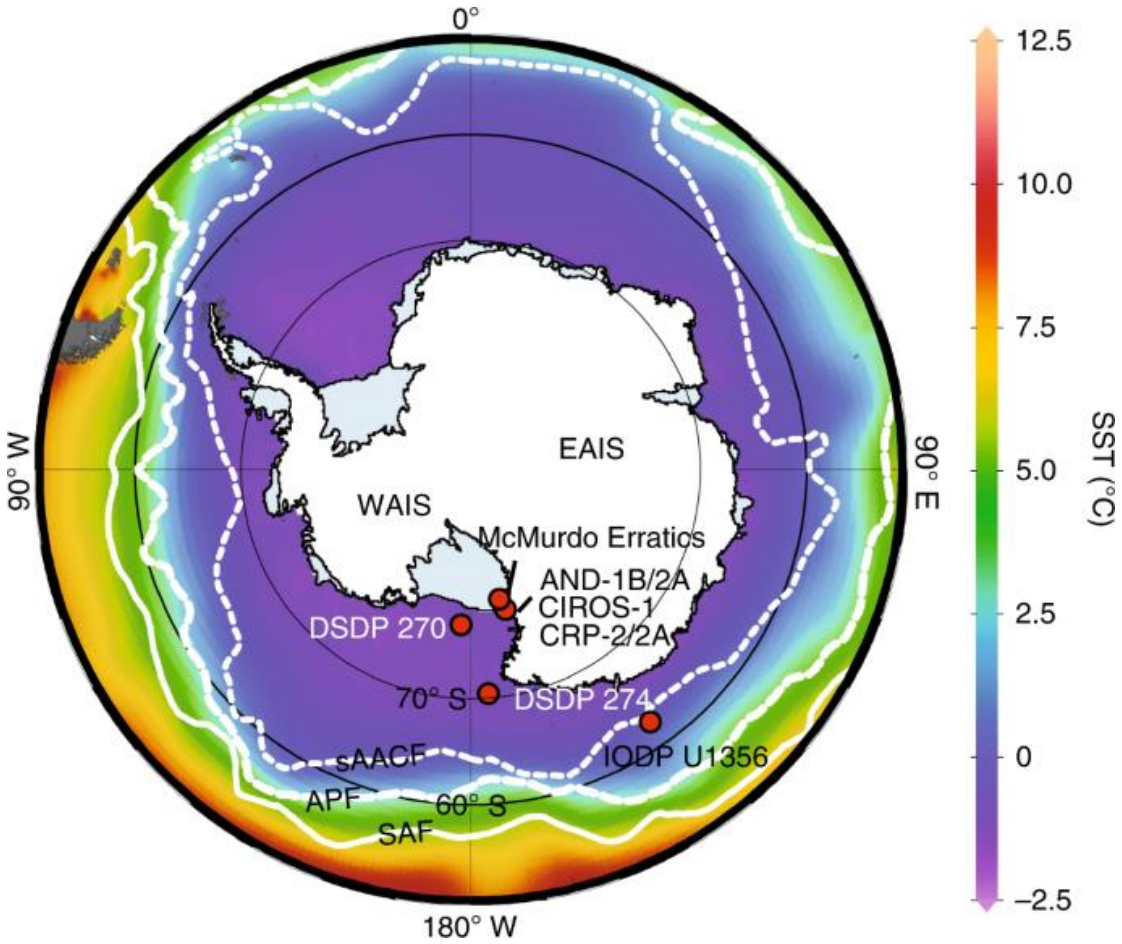

Figure 1. Map of the drill core and sample locations used in this study.

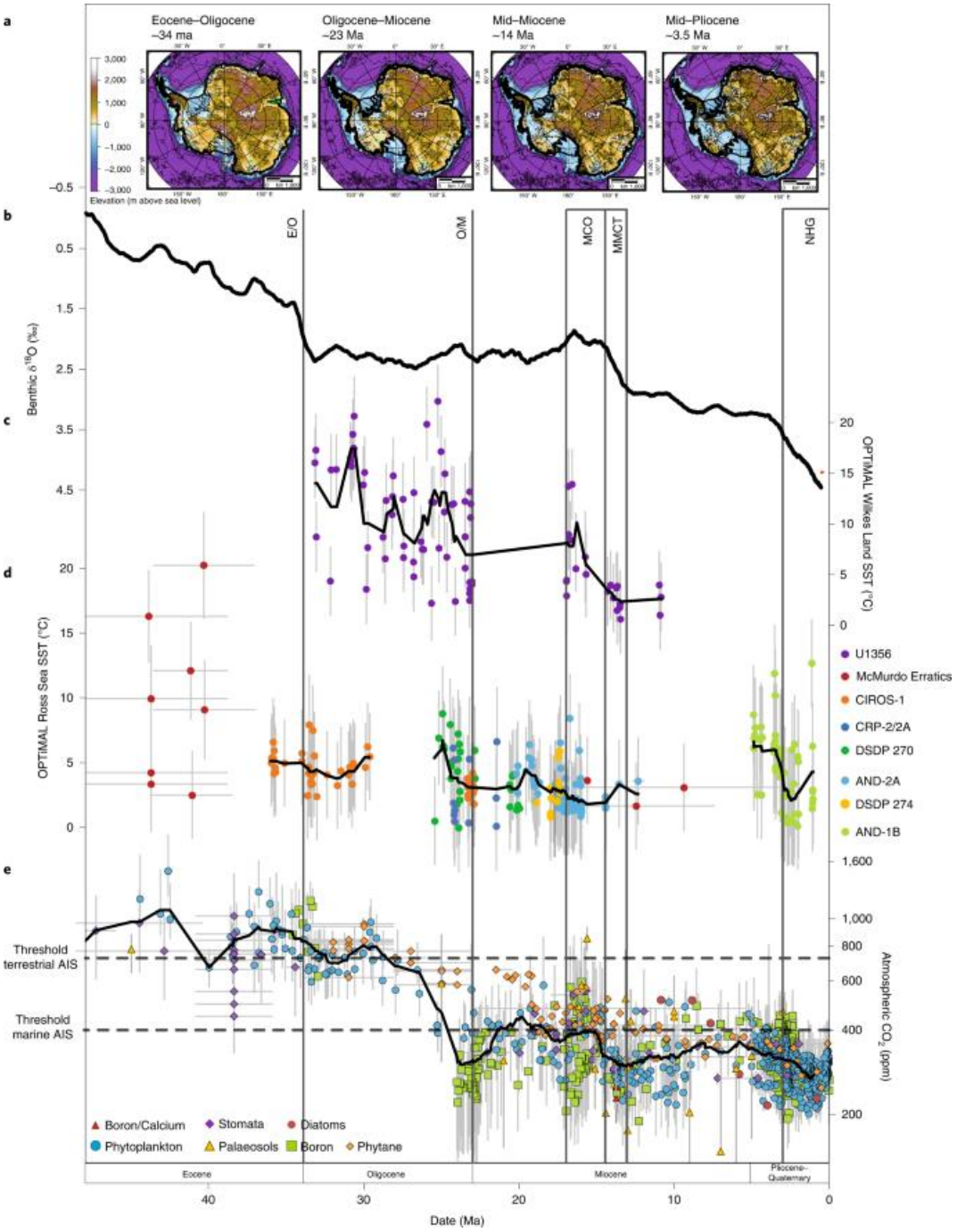

Figure 2. SST compilation from Ross Sea and Wilkes Land sample sites. a, Topographic reconstructions. b, 1 Myr moving average of benthic δ18O stack. c, OPTiMAL SSTs for Site U1356 Wilkes Land have been recalibrated on the basis of GDGT abundances reported previously, d, OPTiMAL SSTs for Ross Sea sample sites. Vertical error bars in c and d represent the standard deviation of the temperature estimate (1σ), while horizontal age errors are described in Methods and Supplementary Data Tables 1–3. Samples with Dnearest values (a weighted distance metric; see Supplementary section 1) above 0.5 have been removed from the compilations. The black lines represent a 1 Myr moving average. e, Atmospheric CO2 concentrations, with the black line representing a 2 Myr moving average (Methods). Dashed horizontal bars represent atmospheric CO2 thresholds for a terrestrial AIS and marine AIS. Vertical bars indicate major climate events; E/O, Eocene/Oligocene boundary; O/M, Oligocene/Miocene boundary; NHG, Northern Hemisphere glaciation.

5. 红海南部海底扩张、信风和降水之间的反馈关系

翻译人：张靖宇 zhangjy6@sustech.edu.cn

Hu Z, Shi Z, Li G, et al. ***Feedbacks between sea-floor spreading, trade winds and precipitation in the Southern Red Sea*** *[J]. Nature Communications, 2022, 13: 5405.*

https://doi.org/10.1038/s41467-022-32293-1

摘要：气候和地质过程之间的反馈是非常有争议的，测试它们是地球科学中的一个关键挑战。阿拉伯红海边缘的大陡崖有几个特征，使其成为研究地表过程对地球深处影响的有效的天然实验室。这些特征包括强烈的地形降雨、凸形河道剖面与西侧的凹形剖面、河道的形态不均衡以及与红海中部深度变化有关的从北到南的系统形态变化。这里我们认为，这些特征可以很好地解释为一个周期，该周期始于红海的扩张，涉及到地形降水、构造变形、大洋扩张和沿海岩浆活动之间的反馈。这种反馈似乎因湿润的东信风而得到加强，东信风与红海的海底扩张基本同时启动。

ABSTRACT: Feedbacks between climatic and geological processes are highly controversial and testing them is a key challenge in Earth sciences. The Great Escarpment of the Arabian Red Sea margin has several features that make it a useful natural laboratory for studying the effect of surface processes on deep Earth. These include strong orographic rainfall, convex channel profiles versus concave swath profiles on the west side of the divide, morphological disequilibrium in fluvial channels, and systematic morphological changes from north to south that relate to depth changes of the central Red Sea. Here we show that these features are well interpreted with a cycle that initiated with the onset of spreading in the Red Sea and involves feedbacks between orographic precipitation, tectonic deformation, mid-ocean spreading and coastal magmatism. It appears that the feedback is enhanced by the moist easterly trade winds that initiated largely contemporaneously with sea floor spreading in the Red Sea.

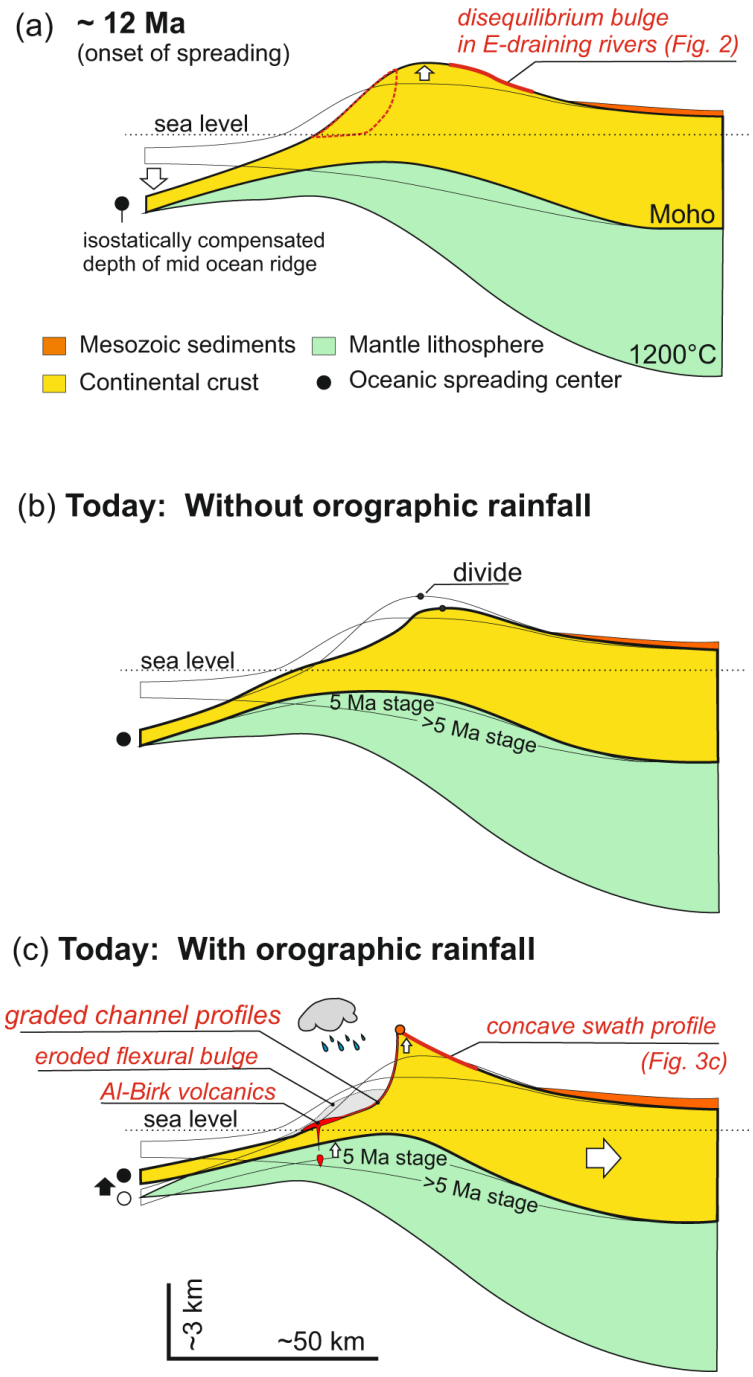

Figure 1. Major steps in the evolution of the Arabian Red Sea margin. a At or near the time of initial formation of oceanic lithosphere. Formation of oceanic lithosphere in Red Sea downwarps margin and creates additional uplift by flexural doming (future erosion dashed red). b, c Evolution since the initial formation of oceanic lithosphere. b Without orographic rain fall. A minor escarpment forms and erosion of uplifted area causes downwearing and backwards mirgrating escarpment with minor flexural rebound in foreland, escarpment not exactly at divide (not realized or only realized in northern, dry part of Red Sea depending on age of spreading there). c With orographic rainfall as for the southern Red Sea coast. Erosion causes additional uplift at escarpment edge, escarpment at divide, decompressional melting in foreland where flexural bulge is eroded softens lithosphere. Flexural lifting of the spreading center occurs.

6. 伊豆-小笠原弧前火山岩钻孔样品的古地磁和古纬度研究---对菲律宾海板块运动的启示

翻译人：刘伟 inewway@163.com

William W S, Claire C. ***Paleomagnetism and paleolatitude of igneous drill core samples from the Izu-Bonin forearc and implications for Philippine Sea plate motion****[J]. Tectonophysics, 2022: 229573.*

https://doi.org/10.1016/j.tecto.2022.229573

摘要：菲律宾海板块是东亚板块的组成部分，但其运动演化只能通过古地磁数据重建。因为该板块大部分位于海底，且几乎没有定向的古地磁数据可用。IODP 352 航次在伊豆-小笠原弧前进行了四个钻孔的取芯，获得了约 1170 m 弧前火成岩，其放射性测年为~51 Ma。对 361 个样品的古地磁测量获得了用于估算古纬度的古磁倾角数据。25 个独立的磁单元显示了 90.1°±4.4°的古余纬度（2σ 的不确定性），这意味着古纬度正好位于赤道上。古纬度变化指示了板块向北漂移了约 28°，这与其他类似年龄的伊豆-小笠原弧前钻孔的古地磁研究一致。钻孔古纬度变化与西菲律宾盆地北向漂移的微小差异与板块的旋转运动一致。部分样品在~30 Ma 后重磁化方向与现今地心轴向偶极子倾角方向一致，指示了一个起源不明的构造事件。

ABSTRACT: The Philippine Sea plate is an integral part of the east Asian plate mosaic but its past motions can only be reconstructed from paleomagnetic data. Moreover, because the plate is largely submarine, few fully-oriented paleomagnetic data are available. International Ocean Discovery Program (IODP) Expedition 352 cored at four sites on the Izu-Bonin forearc, penetrating ~1170 m of forearc igneous crust radiometrically dated at ~51 Ma. Paleomagnetic measurements on 361 samples produced paleo-inclination data that were used to estimate paleolatitude. Twenty five independent magnetic units give a paleocolatitude of 90.1° ±4.4° (2σ uncertainty), implying a paleolatitude exactly on the equator. Unit variance agrees with global paleosecular variation models, implying that these variations have been properly sampled and averaged. The paleolatitude implies northward drift of ~28°, which agrees with other Izu-Bonin forearc sites of similar age. A slight difference in northward drift with West Philippine Basin sites is consistent with plate rotation.

Certain parts of the cored sections yield samples that were remagnetized to the present geocentric axial dipole inclination after ~30 Ma, implying a tectonic event of unclear origin.

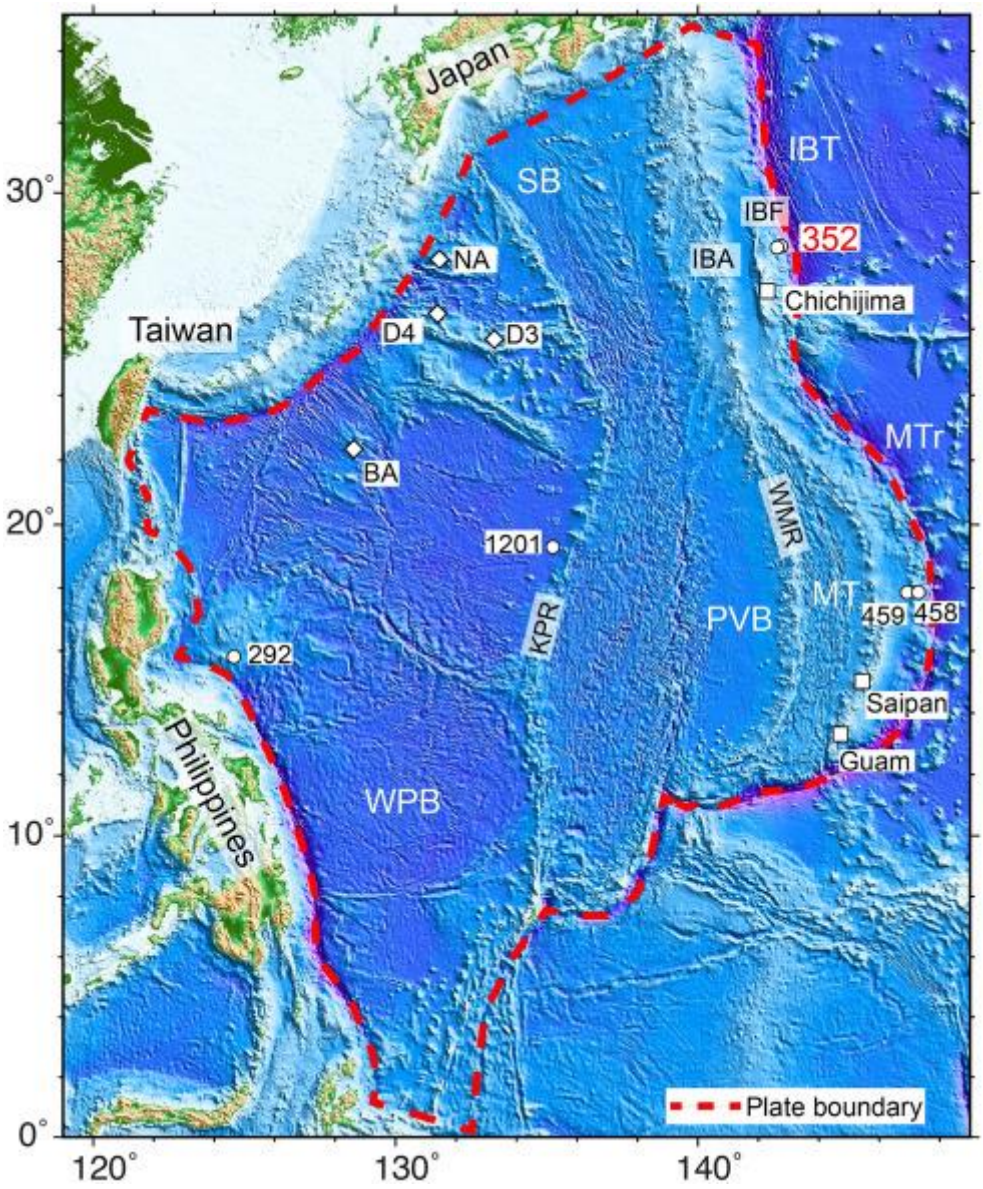

Figure 1. Map of the Philippine Sea plate and sites/core names mentioned in text. Red text indicates Expedition 352 site locations. Open circles mark drill core sites, open diamonds show seafloor drill sites, and open squares denote land sites. Numbers or letters identify data, given in Table 2. Red dashed line is approximate plate boundary (Hall et al., 1995a; Zahirovic et al., 2014). Feature name abbreviations: IBA = Izu-Bonin arc; IBF = Izu-Bonin forearc; IBT = Izu-Bonin Trench; KPR = Kyushu-Palau Ridge; MT = Mariana Trough; MTr = Mariana Trench; PVB = Parece Vela Basin; SB = Shikoku Basin; WMR = West Mariana Ridge; WPB = West Philippine Basin.

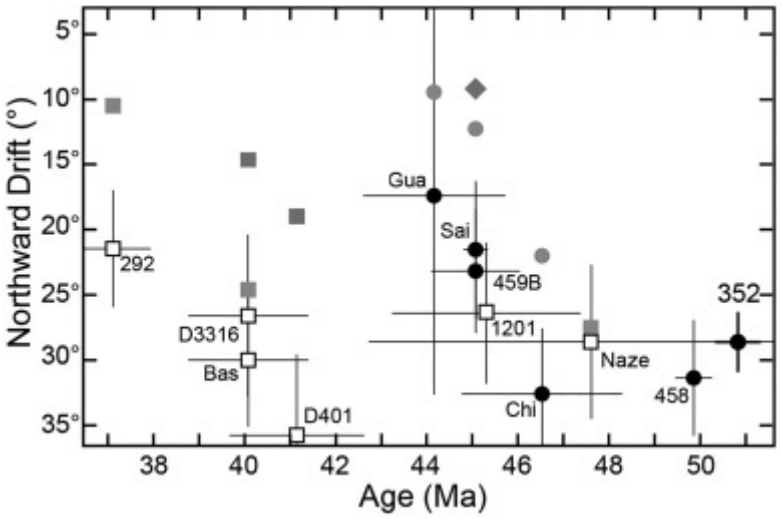

Figure 2. Northward drift indicated by PSP Eocene paleomagnetic data (Table 2) plotted versus age. Open squares indicate sites from the West Philippine Basin and filled circles represent sites from the Izu-Bonin-Mariana arc. Open and black-filled symbols indicate maximum northward drift for each datum, whereas gray symbols show the minimum northward drift. Thin vertical lines indicate standard error uncertainty in paleolatitude. Horizontal thin lines represent age uncertainty.

7. 早维塞尔冰期基于石笋记录的欧洲西风带的漂移在 MIS5a 期间存在百年尺度变化

翻译人：杨会会 11849590@mail.sustech.edu.cn

Kim D, Kim H J, Kang S M, et al., ***Weak Hadley cell intensity changes due to compensating effects of tropical and extratropical radiative forcing [J].*** *Climate and atmospheric science. 2022,5, 61.*

https://doi.org/10.1016/j.quascirev.2022.107581

摘要：维塞尔冰期的特征是海洋环流的显著变化，始于~115 ka，终止于~11.5 ka。维塞尔冰期早期，特别是在深海氧同位素 (MIS) 5a 阶段：85-74ka，为认识欧洲西风带与地中海气候之间的联系提供了一个窗口。然而，缺乏具有绝对年代学的高分辨率古气候记录，阻碍了我们对地中海周边地区十年-百年尺度上气候变化及其驱动的认识。本文介绍了摩纳哥 Observatoire 洞穴(43° 44′ N, 7° 25′ E)，基于石笋 230Th 定年结果的水文气候记录，时间范围为 88.7±0.4～80.3±0.1 ka，覆盖了 MIS 5b 和 5a 的部分阶段。Observatoire 洞和地中海周围石笋记录之间的一致证实了大西洋-欧洲地区在从 MIS 5b 到 5a 过渡期间的大规模变暖。次年代际分辨率的 Observatoire 洞 δ 18O 和 δ 13C 记录在 MIS 5a 前半期，即 84-80 ka 揭示了欧洲南部存在 4 个跨百年尺度（multi-centennial）的干旱期，表明存在百年尺度的西风漂移，这一发现得到了模式模拟的支持。西风带的变化和相关的干旱事件可归因于大西洋经向翻转环流的减缓、北大西洋涛动状态和太阳活动。

ABSTRACT: The Weichselian glaciation is characterized by significant ocean circulation variations starting from ~115 thousand years ago (ka) and terminating at ~11.5 ka. The early Weichselian (115-74 ka), especially marine isotope stage (MIS) 5a at 85-74 ka, provides a window for understanding the linkage between the European westerlies and Mediterranean climate. However, lack of highly-resolved paleoclimate records with absolute chronologies hampers our knowledge of decadal-to-centennial-scale climate changes and forcings in the circum-Mediterranean realm. Here, we present 230Th-dated stalagmite inferred hydroclimate records from Observatoire cave (43° 44′ N, 7° 25′ E), Monaco, for the period between 88.7 ± 0.4 and 80.3 ± 0.1 ka, covering

portions of MIS 5b and 5a. Agreement between Observatoire and circum-Mediterranean stalagmite records confirm large-scale warming over the Atlantic-Europe territory during the transition from MIS 5b to 5a. Subdecadally-resolved Observatoire δ18O and δ13C records express four multi-centennial arid intervals in southern Europe at 84-80 ka in the first-half of MIS 5a, suggesting centennial westerly drifts, a finding supported by a model simulation. Westerly changes and associated arid events can be attributed to slowdowns of the Atlantic meridional overturning circulation, North Atlantic Oscillation states, and solar activity.

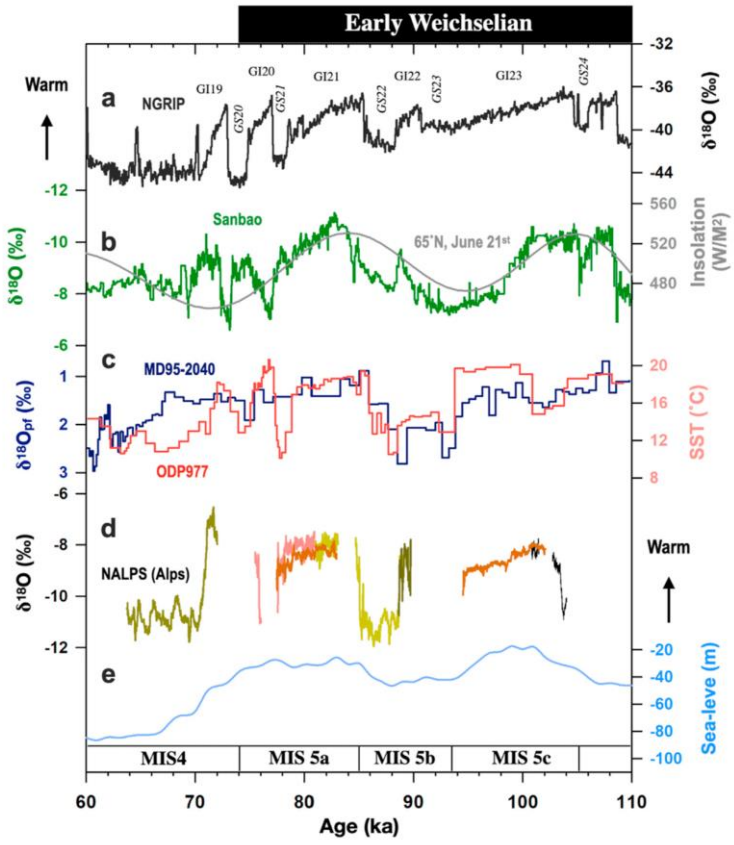

Figure 1. Paleoclimate records during the early Weichselian. (a) δ18O values in NGRIP Greenland ice core (North GRIP-Members, 2004). High δ18O values imply warm climate in the N Atlantic. GI: Greenland interstadial. GS: Greenland stadial. (b) Grey: North hemisphere insolation at 65°N, June 21st (Laskar et al., 2011). Green: Stalagmite δ18O from Sanbao cave, China, as a proxy for Asian summer monsoon intensity (Cheng et al., 2016). Negative δ18O values represent a strong Asian summer monsoon. (c) Orange: sea surface temperature (SST) from marine core ODP 977 at Iberia (Martrat et al., 2004). Dark blue: Planktonic foraminiferal δ18O (δ18O pf) from marine core MD 95-2040 (de Abreu et al., 2003). (d) Stalagmite δ18O from the Alps (NALPS) (Boch et al., 2011). High δ18O values indicate warm conditions. (e) Global stacked sea level record (Spratt and Lisiecki, 2016). (For interpretation of the references to color in this figure legend, the reader is referred to the Web version of this article).

8. 保存完好的克拉通间岩石圈揭示澳大利亚的元古代拼合

翻译人：曹伟 11930854@qq.com

Lu Y, Wingate M, Smithies R. ***Preserved intercratonic lithosphere reveals Proterozoic assembly of Australia*** *[J]. Geology, 2022.*

https://doi.org/10.1130/G50256.1

摘要：澳大利亚的元古宙拼合，其理解对于重建元古宙超大陆至关重要，涉及西澳大利亚（WAC）、北澳大利亚（NAC）和南澳大利亚克拉通（SAC）的拼合。然而，这些太古宙至早元古代岩石圈块体之间的基底大多埋藏在较年轻的盆地下方；因此，其组成和年龄以及元古代拼合的时间仍然不确定。本研究对穿过坎宁盆地西北部基底的钻孔中火成岩进行的原位锆石 U-Pb-O-Hf 分析表明，在 WAC 和 NAC 之间存在大量的新生元古代岩石圈区域，即珀西瓦尔湖区。尽管与邻近的 WAC 和 NAC 同位素不同，但珀西瓦尔湖区域与 WAC、NAC 和 SAC 之间的其他年轻元古代构造元素惊人地相似。结合同位素和地震数据，我们将珀西瓦尔湖区域解释为约 1700×400 km 元古代岩石圈区域的一部分，该区域缺乏太古宙物源证据，但主要由在 WAC-NAC-SAC 汇聚中保留的中元古代洋壳的改造残余物组成。克拉通之间明显缺乏太古宙岩石圈，这意味着它们从未直接碰撞，或者是聚合的岩石圈块体中三维海隆的碰撞阻止了完全碰撞。相反，珀西瓦尔湖区域和 WAC、NAC 和 SAC 之间的其他元古代元素由从元古代地幔提取的海洋岩石圈组成。我们的结果表明，WAC-NAC 汇聚比哥伦比亚拼合作用年轻约 1.8 Ga，元古代澳大利亚形成于罗迪尼亚组合的最早阶段，约 1.3 Ga。

ABSTRACT: The Proterozoic assembly of Australia, the understanding of which is critical for reconstructing Proterozoic supercontinents, involved amalgamation of the West Australian (WAC), North Australian (NAC), and South Australian cratons (SAC). However, the basement between these Archean to early Proterozoic lithospheric blocks is mostly buried beneath younger basins; hence, its composition and age and the timing of Proterozoic assembly remain uncertain. In situ zircon U-Pb-O-Hf analyses of igneous rocks from drillholes that intersected basement beneath the northwestern Canning Basin reveal the presence of a substantial domain of juvenile Proterozoic lithosphere, the Percival Lakes province, between the WAC and NAC. Although isotopically

distinct from the neighboring WAC and NAC, the Percival Lakes province is strikingly similar to other juvenile Proterozoic tectonic elements between the WAC, NAC, and SAC. Combining isotope and seismic data, we interpret the Percival Lakes province as part of an ~1700×400 km Proterozoic lithospheric domain that lacks evidence of Archean provenance but consists mainly of reworked remnants of Mesoproterozoic oceanic crust that survived WAC-NAC-SAC convergence. The apparent absence of Archean lithosphere between the cratons implies they never directly collided or that complete collision was prevented by impingement of three-dimensional promontories in the converging lithospheric blocks. Instead, the Percival Lakes province and other Proterozoic elements between the WAC, NAC, and SAC consist of oceanic lithosphere extracted from Earth s mantle in the Proterozoic. Our results imply that WAC-NAC convergence was younger than Columbia amalgamation at ca. 1.8 Ga and that Proterozoic Australia formed during the earliest phases of Rodinia assembly at ca. 1.3 Ga.

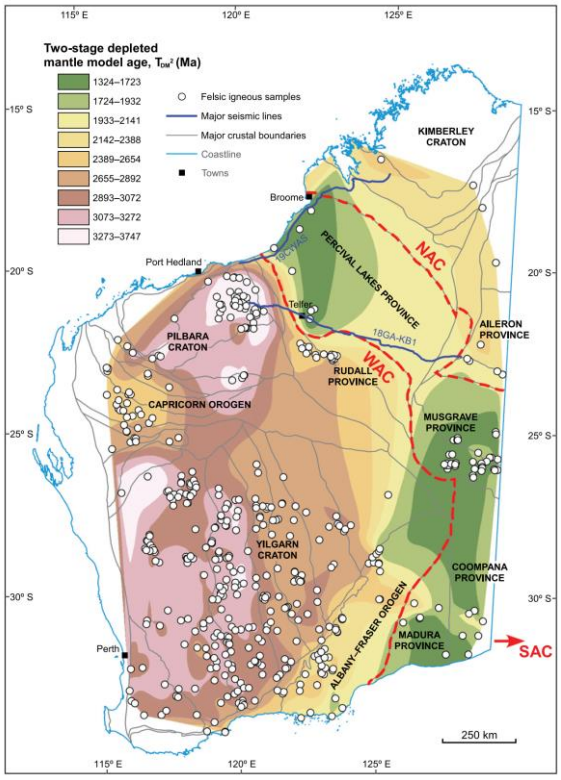

Figure 1. Zircon Lu-Hf isotope map for felsic igneous rocks in Western Australia, based on the median two-stage depleted mantle model age (TDM2), calculated using the depleted mantle model of Vervoort et al. (2018). Red dashed lines separate the West Australian craton (WAC) and North Australian craton (NAC) from the intervening Proterozoic lithosphere. Major crustal boundaries are from Martin et al. (2022). SAC South Australian craton. Major seismic lines in the Percival Lakes province (PLP) include 18GA-KB1 (Doublier et al., 2020) and 19CWAS (Zhao et al., 2022). Sample locations can be found at the Government of Western Australia website.

9. 上新世晚期南亚季风变化和北极海冰范围关系

翻译人：王浩森 11930841@mail.sustech.edu.cn

Behera P, Tiwari M, Kumar V, et al. ***South Asian Monsoon variability and Arctic sea ice extent linkages during the late Pliocene****[J]. Paleoceanography and Paleoclimatology, e2022PA004436.*
https://doi.org/10.1029/2022PA004436

摘要：气候变暖导致北极海冰范围（SIE）减少对南亚季风（SoAM）的影响尚不清楚。中上新世暖期（MPWP，3.264-3.0.5 百万年前，Ma）是最近的二氧化碳水平与现在相似的暖期事件，被认为是未来全球变暖的模型。我们利用来自阿拉伯海东部的反硝化、生产力、风化和陆源输入记录（国际海洋发现计划第 355 航次），提出了多个高分辨率记录指示上新世晚期 SoAM 变化的(~3.4–2.7 Ma)。利用混合模型代理数据集（Oscillayers），我们确定了 MPWP 期间和 2.9 Ma 期间季风增强的两个不同间隔。SoAM 变化似乎是动力学（日照、北极 SIE 变化和印度尼西亚通流变化导致的南热带印度洋表面温度变化）和热力学效应（pCO2 变化导致的全球温度变化）之间的相互作用的结果。利用上新世晚期北极春季海冰浓度重建，我们发现，较低（较高）的北极 SIE 通过不对称的半球间能量输出和通过调节急流流和经向环流，导致上新世后期更强（较弱）的 SoAM。在 MPWP 期间，我们发现 SoAM 增强，这证实了模型结果，并意味着随着气候持续变暖，预计南亚将出现更强烈的降水。

ABSTRACT: The influence of a warming-induced reduction in Arctic sea ice extent (SIE) on the South Asian monsoon (SoAM) is not well understood. The mid-Piacenzian Warm Period (MPWP, 3.264–3.025 million years ago, Ma), the most recent warm climate event when the Earth's CO2 levels were similar to the present, is considered an analog for future global warming. We present a multi-proxy high-resolution record of SoAM variability during the late Pliocene (~3.4–2.7 Ma) using denitrification, productivity, weathering, and terrestrial influx proxies from the eastern Arabian Sea (International Ocean Discovery Program Expedition 355). The proxy-based SoAM reconstruction is independently verified using a hybrid model-proxy data set (Oscillayers). We identify two distinct intervals of monsoon intensification—during the MPWP and at 2.9 Ma. The SoAM variability appears to result from an interplay between dynamic (Insolation, Arctic SIE

variability, and southern tropical Indian Ocean surface temperature variability due to Indonesian Throughflow changes) and thermodynamic effects (global temperature change due to pCO2 variability). Using a late Pliocene Arctic spring sea ice concentration reconstruction, we find that lower (higher) Arctic SIE leads to stronger (weaker) late Pliocene SoAM via asymmetric interhemispheric energy export and through modulating jet stream flow and meridional circulation. Our finding of strengthened SoAM during the MPWP corroborates model results and implies that

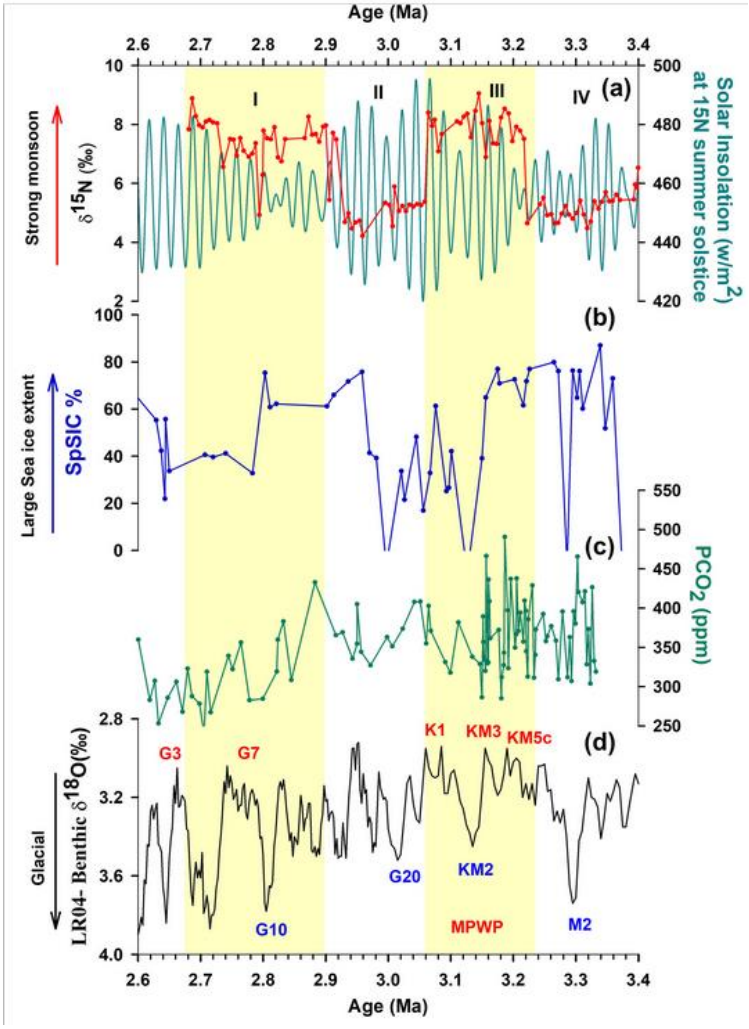

more intense precipitation is expected over South Asia with continued climate warming.

Figure 1. Forcing factors of South Asian monsoon (SoAM) variability during late Pliocene. (a) Solar insolation at 15°N summer solstice plotted with the Site U1456 SoAM intensity record (δ15N); (b) Spring sea ice cover (SpSIC%) from the Yermak Plateau (Ocean Drilling Program (ODP) 151, Site 910C) reflects Arctic sea ice extent during the late Pliocene; (c) The atmospheric CO2 concentrations derived from boron isotope (δ11Bborate) of G. ruber from the ODP Site 999, Caribbean Sea; (d) LR04 benthic foraminifer δ18O (‰) stack shows glacial-interglacial cycles. The yellow bands show periods of enhanced monsoon.

10. 北大西洋古新世-始新世极热期内外巨型磁化石的发现

翻译人：王敦繁 Dunfan-w@foxmail.com

Xue, P., Chang, L., Pei, Z., Harrison, R. J. ***Discovery of giant magnetofossils within and outside of the Palaeocene-Eocene Thermal Maximum in the North Atlantic [J]****, Earth and Planetary Science Letters, 584, 2022, 117-417,*

https://doi.org/10.1016/j.epsl.2022.117417

摘要：与传统的生物成因磁性纳米颗粒相比，巨磁化石具有异常大的颗粒尺寸和独特的形貌。这些不同寻常的磁性晶体的起源是一个谜，因为现代没有发现已知的类似磁性化石。迄今为止，巨型磁化石是在过去变暖时期沉积的海洋沉积物中发现的，这导致人们认为这些化石与古代的高温事件唯一有关。在这里，我们报道了在北大西洋 IODP 钻孔 U1403 和 U1409 远洋沉积物中不同深度的巨型磁化石，结果表明不仅在古新世-始新世热峰值(PETM;~ 56 Ma)的间隔期有丰富的巨型磁化石出现，也在 PETM 之前(比古新世-始新世边界早 700 千年，)和 PETM 之后(比古新世-始新世边界晚 300 千年)，以及在~ 70 Ma 沉积物中有丰富的巨型磁化石出现。我们的研究结果表明，巨型生物成因磁铁矿晶体并不是在古代高温事件中唯一产生的。我们还利用尺寸分析和微磁模拟研究了巨型磁铁矿颗粒的磁畴状态。形态学、成分和晶体学特征，探讨了这些不寻常晶体的潜在生物起源。

ABSTRACT: Giant magnetofossils have exceptionally large grain sizes and peculiar morphologies compared to conventional biogenic magnetite nanoparticles. The origin of these unusual magnetic crystals is a mystery because there are no known modern analogues. Giant magnetofossils have so far been identified in marine sediments deposited during past warming periods, leading to the assumption that these fossils were uniquely tied to ancient hyperthermal events. Here we describe the occurrence of abundant giant magnetofossils within North Atlantic pelagic sediments from International Ocean Discovery Program (IODP) Sites U1403 and U1409 at distinct palaeodepths not only during the Palaeocene-Eocene Thermal Maximum (PETM; ~56 Ma) intervals but also far before (>700 ky earlier than the PEB, Palaeocene- Eocene boundary) and after (>300 ky later than the PEB) the PETM, and in a sample of ~70 Ma age. Our results indicate that giant biogenic magnetite crystals were not uniquely produced during ancient hyperthermal events. Magnetic

domain states of giant magnetite particles are investigated using dimensional analysis and micromagnetic simulations. Morphological, compositional, and crystallographic data point towards a potential biogenic origin of those unusual crystals.

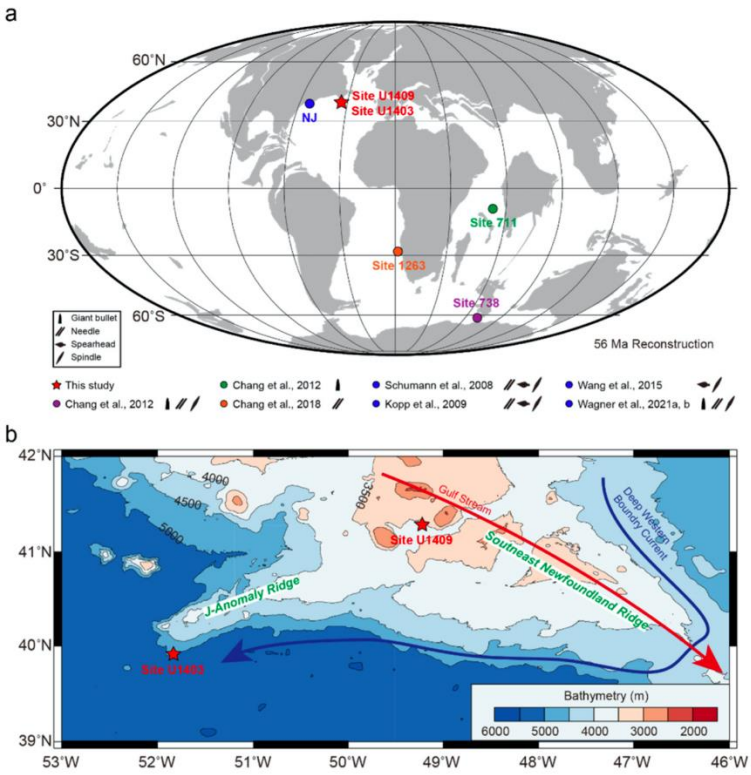

Figure 1. Location of the studied IODP sites (U1403 and U1409) from the North Atlantic. (a) A map of plate tectonic reconstruction at 56 Ma obtained from the Ocean Drilling Stratigraphic Network (ODSN) database (http://www.odsn.de). Red stars represent the site location in this study. Solid circles of different colors show the site location from previous studies that identified giant magnetofossils. The small cartoon drawings of four different solid shapes represent giant bullet, needle, spearhead, and spindle, respectively. NJ, New Jersey. (b) Current bathymetric map of the studied site area. Bathymetric data are from the National Oceanic and Atmospheric Administration (NOAA). Blue and red arrows represent Deep Western Boundary Current and Gulf Stream, respectively. (For interpretation of the colors in the figure(s), the reader is referred to the web version of this article.)

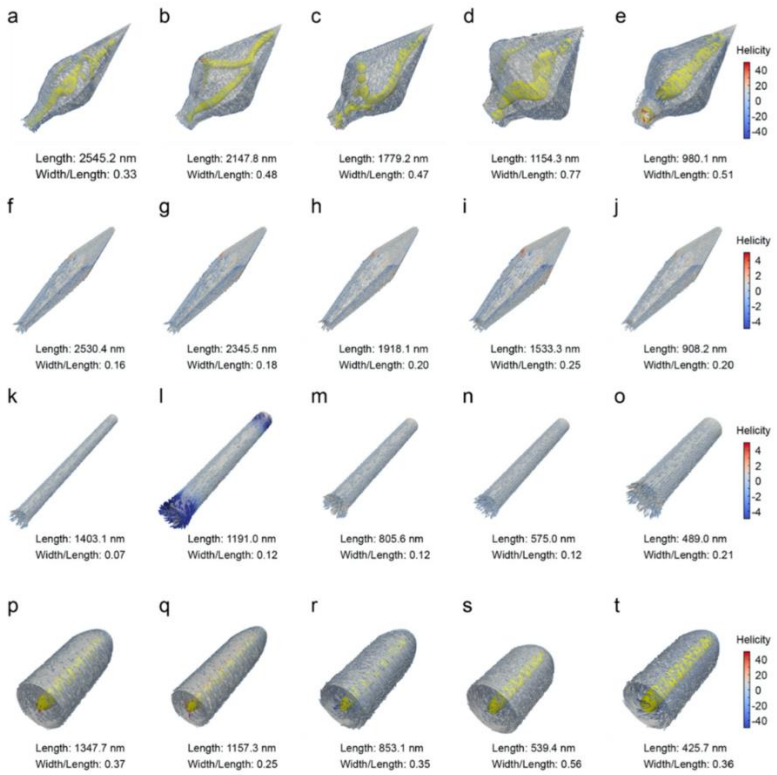

Figure 2. Micromagnetic simulations of magnetic domain states for typical observed giant magnetite crystals of variable morphologies and sizes. The domain structures of saturated isothermal remanent magnetization are calculated along the axis parallel to the crystal elongation direction. (a-e) MD structure of all spearheads. (f-j) SD structure of all spindles. (k-o) SD structure of all needles. A needle of 1191 nm length with a width/length ratio of 0.12 shows a vortex structure at the ends of the particle (l). (p-t) Single vortex domain structure of all giant bullets. The crystal length and width/length ratio of each particle are indicated. Arrows showing magnetic moments were colored by helicity. Yellow surfaces show vortex cores.

11. 大陆溢流玄武岩驱动显生宙生物灭绝

翻译人：张伟杰 12031188@mail.sustech.edu.cn

Green T, Renne P R, Keller C B. ***Continental flood basalts drive Phanerozoic extinctions****[J]. Proceedings of the National Academy of Sciences, 2022, 119(38): e2120441119.*

https://doi.org/10.1073/pnas.2120441119

摘要：放射性定年技术精确度和准确度的提高推动了地质年代划分的优化，揭示了大火成岩省（LIPs）与显生宙动物群更替之间的明显相关性，相关内容在定性层面上已经讨论了很多。然而，由于许多大规模灭绝都有其他的致死机制，这种相关性在多大程度上可能是偶然发生的还有待定量测试。本文，我们展示了显生宙陆相 LIPs 和动物群更替之间的时间相关性不太可能是偶然，这表明灭绝和陆相溢流玄武岩之间存在因果关系。对于喷发速率较高 LIPs 和灭绝程度较高的地质年代界限，这种关系更强。这表明 LIP 岩浆脱气可能释放的 CO2、SO2、Cl 和 F 等是物种大规模灭绝和其他时期动物群更替的主要致死机制。我们的研究结果表明，陆相大灭绝是显生宙物种灭绝的主要直接驱动因素。

ABSTRACT: Refinements of the geological timescale driven by the increasing precision and accuracy of radiometric dating have revealed an apparent correlation between large igneous provinces (LIPs) and intervals of Phanerozoic faunal turnover that has been much discussed at a qualitative level. However, the extent to which such correlations are likely to occur by chance has yet to be quantitatively tested, and other kill mechanisms have been suggested for many mass extinctions. Here, we show that the degree of temporal correlation between continental LIPs and faunal turnover in the Phanerozoic is unlikely to occur by chance, suggesting a causal relationship linking extinctions and continental flood basalts. The relationship is stronger for LIPs with higher estimated eruptive rates and for stage boundaries with higher extinction magnitudes. This suggests LIP magma degassing as a primary kill mechanism for mass extinctions and other intervals of faunal turnover, which may be related to CO2, SO2, Cl, and F release. Our results suggest continental LIPs as a major, direct driver of extinctions throughout the Phanerozoic.

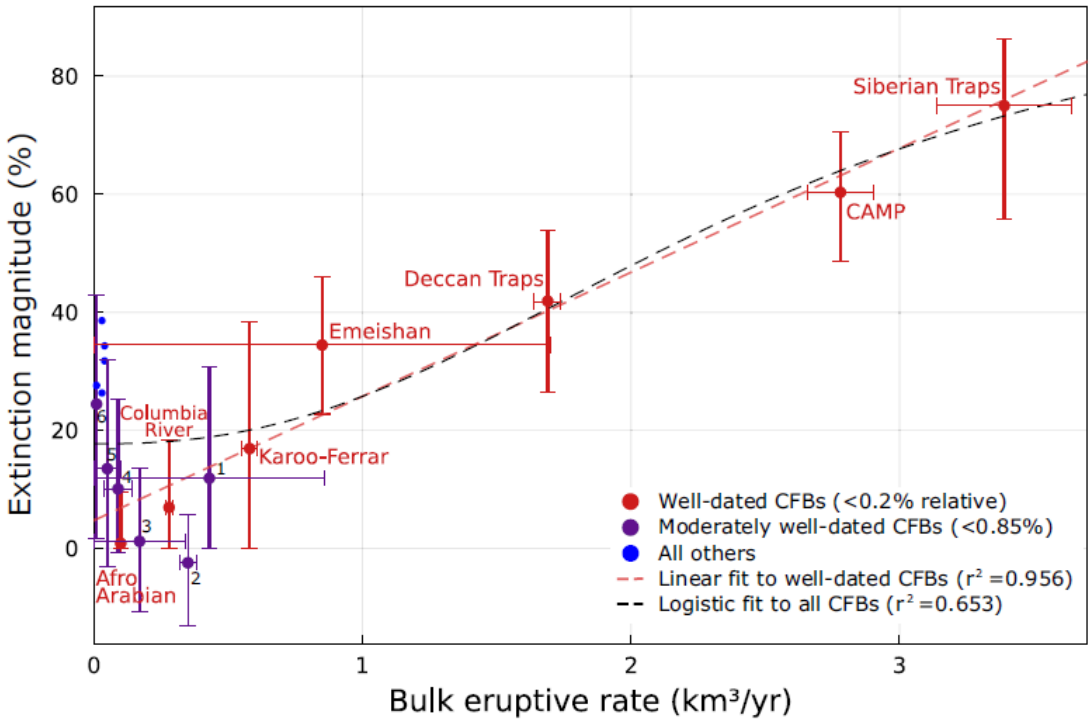

Figure 1. CFB bulk eruptive rates correlate strongly with extinction severity.

12. 气候网络曲率解释的不同厄尔尼诺类型遥相关模式

翻译人：李海 12031330@mail.sustech.edu.cn

Strnad F M, Schlör J, Fröhlich C, et al. ***Teleconnection patterns of different El Niño types revealed by climate network curvature*** *[J]. Geophysical Research Letters, 2022, 49, e2022GL098571.*

https://doi.org/10.1029/2022GL098571

摘要：厄尔尼诺事件的多样性通常由东太平洋（EP）和中太平洋（CP）两种不同类型来描述。虽然对 EP 和 CP 事件的远程影响（即遥相关）已经分别在不同区域进行了研究，但对它们的结果仍缺乏全局的了解。在本研究中，作者使用应用在由地表气温数据构建的气候网络的 Forman-Ricci 曲率来区分区域链接与遥相关。研究结果表明，两种厄尔尼诺类型都会影响遥相关模式，但具有不同的空间表现形式。分析结果表明 EP 厄尔尼诺现象改变了大气环流，从而将遥相关结构改变为主要的热带遥相关。相比之下，CP 厄尔尼诺现象的遥相关模式仅显示正常条件的细微变化。此外，这项工作将东太平洋的动态确定为两种厄尔尼诺类型的远程影响的代理。

ABSTRACT: The diversity of El Niño events is commonly described by two distinct flavors, the Eastern Pacific (EP) and Central Pacific (CP) type. While the remote impacts, i.e., teleconnections, of EP and CP events have been studied for different regions individually, a global picture of their structure is still lacking. Here, we use Forman-Ricci curvature applied on climate networks constructed from surface air temperature data to distinguish regional links from teleconnections. Our results confirm that both El Niño types influence the teleconnection patterns, however, with different spatial manifestations. Our analysis suggests that EP El Niños alter the general circulation which changes the teleconnection structure to primarily tropical teleconnections. In contrast, the teleconnection pattern of CP El Niños show only subtle changes to normal conditions. Moreover, this work identifies the dynamics of the Eastern Pacific as a proxy for the remote impact of both El Niño types.

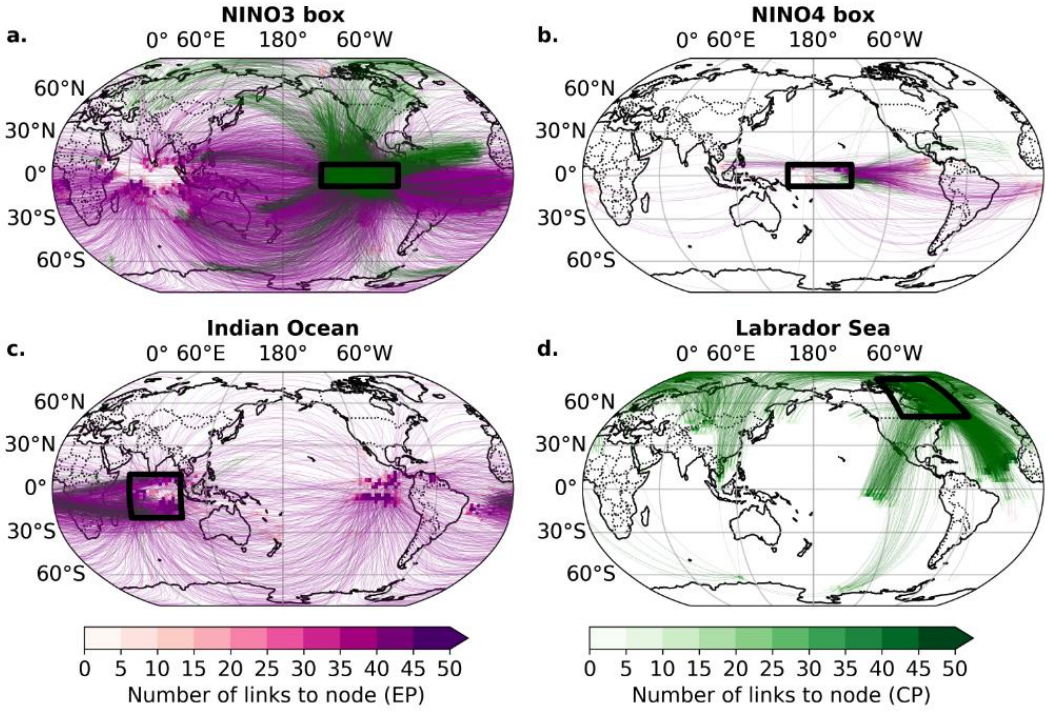

Figure 1. Teleconnections from eastern and Central Pacific Ocean, IO, and the Labrador Sea. F−ij, i.e., teleconnections, for EP (purple) and CP (green) El Niño events connected to the four selected regions (black rectangles): Niño 3 (a), Niño 4 (b), IO (c), and Labrador Sea (d). For visual clarity, only a third of all links are shown.

13. 地中海东部末次间冰期十年际尺度海表温度变化

翻译人：张亚南 zhangyn3@mail.sustech.edu.cn

Obreht I., Vleeschouwer, D.D., Wörmer, L., et al. Last Interglacial decadal sea surface temperature variability in the eastern Mediterranean [J] Nature Geoscience, 2022.

https://doi.org/10.1038/s41561-022-01016-y

摘要：末次间冰期（约 129,000-116,000 年前）是距今最近的地质历史时期，气候比现今气候更加温暖。通过这一区间基于温度替代指标重建可以帮助我们理解当前自然气候变率背景变暖的世界，特别是定义十年际尺度的气候变化。本文作者通过地中海东部细层状富有有机质腐泥层进行长链烯酮的光谱成像技术重建一个大约 4800 年的海表温度记录。作者观测到年代际变化幅度最高的是腐殖质沉积的早期阶段，可能是由于水团分层作用增强导致的垂向混合作用减弱导致的。而在腐泥沉积后期，当海温强迫与现今环境相似时，我们观测到最大重建的年代际变率振幅没有超过最近气候变暖期的范围。从最近百年海温趋势表明，我们最后一次间冰期记录的最大百年尺度海温增加低于预计二十一世纪的气温变暖。

ABSTRACT: The Last Interglacial (~129,000–116,000 years ago) is the most recent geologic period with a warmer-than-present climate. Proxy-based temperature reconstructions from this interval can help contextualize natural climate variability in our currently warming world, especially if they can define changes on decadal timescales. Here, we established a ~4.800-year-long record of sea surface temperature (SST) variability from the eastern Mediterranean Sea at 1–4-year resolution by applying mass spectrometry imaging of long-chain alkenones to a finely laminated organic-matter-rich sapropel deposited during the Last Interglacial. We observe the highest amplitude of decadal variability in the early stage of sapropel deposition, plausibly due to reduced vertical mixing of the highly stratified water column. With the subsequent reorganization of oceanographic conditions in the later stage of sapropel deposition, when SST forcing resembled the modern situation, we observe that the maximum amplitude of reconstructed decadal variability did not exceed the range of the recent period of warming climate. The more gradual, centennial SST trends reveal that the maximal centennial scale SST increase in our Last Interglacial record is below

the projected temperature warming in the twenty-first century.

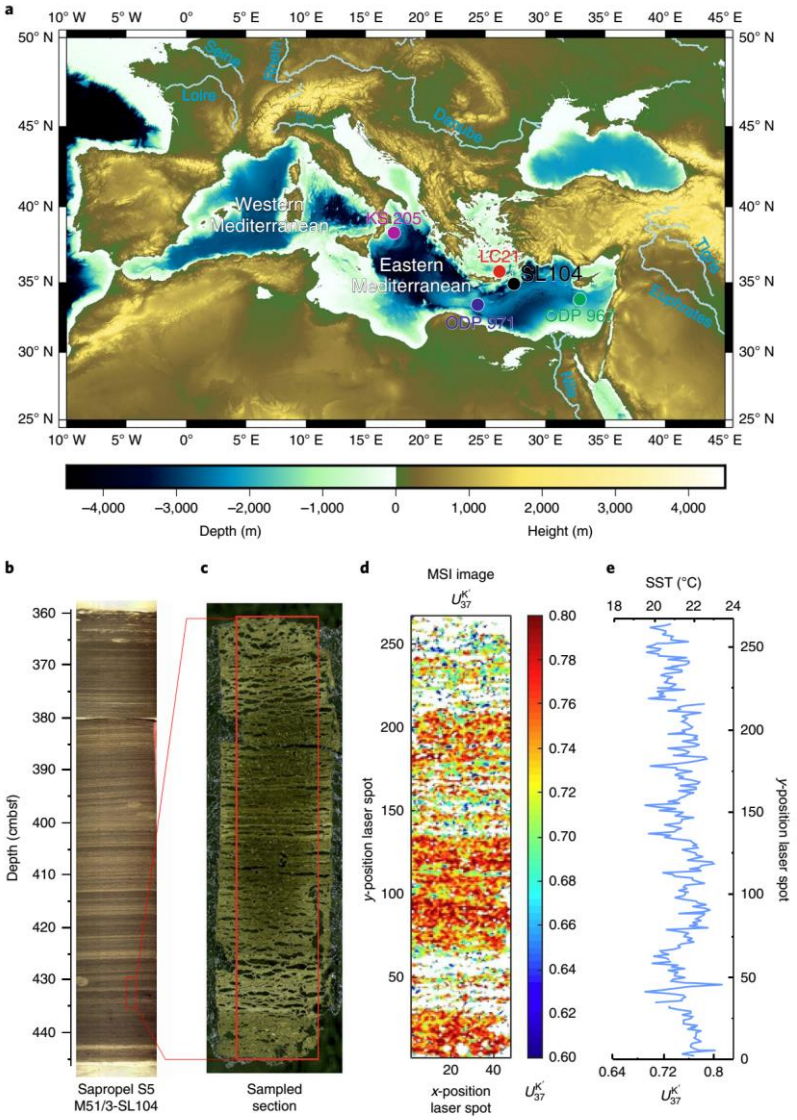

Figure 1. Location and stratigraphy of sapropel S5 and an exemplary MSI-based determination of SST via analysis of alkenones. a, Map of the Mediterranean Sea; the map was generated by The Generic Mapping Tools software. Core M51/3-SL104 is indicated with a black circle. Discussed cores from the eastern Mediterranean with preserved sapropel S5 and alkenone-based SST reconstruction (LC21 21, ODP Site 971 28, ODP Site 96728, KS 20528) are indicated with coloured circles. b, Sapropel S5 from core M51/3-SL104; sediment depth is presented in centimetres below seafloor (cmbsf). c – e, An illustrative example of MSI on a ~5 cm embedded subsample. c, Image of a slice on which MSI was performed, red rectangle indicates the area analysed. d, Spatial distribution of UK37′ values obtained by MSI. Note that the scale is presented as x- and y-position spot, where each spot accounts for 200 µm. e, UK′ 37 and calculated SST time series for the selected sample; data points represent SST derived from UK37′ values calculated from the sum of alkenone intensities in one horizontal layer (only layers with >10 spots with successful detection of alkenones were considered). Depth is presented as y-position spots where each spot is 200 µm.

14. 过去半个世纪全球海洋热量吸收的驱动力和分布

翻译人：夏文月 12231072@mail.sustech.edu.cn

Huguenin, M. F., Holmes, R. M., & England, M. H. ***Drivers and distribution of global ocean heat uptake over the last half century.*** *Nature Communications. 2022, 13(1), 4921.*
https://doi.org/10.1038/s41467-022-32540-5

摘要：自 20 世纪 70 年代以来，海洋吸收了地球系统中由于温室变暖而增加的几乎所有的额外能量。然而观测的不足限制了我们对海洋吸收热量（OHU）发生的地点和如今热量储存地点的了解。本文中，我们平衡了一个重新分析强迫的大洋海冰模型，利用了一个在早期方法基础上改进的自旋加快模型，逐个盆地地去调查最近的 OHU 趋势，并与表面风的趋势、热力学特性（温度、湿度和辐射）或两者分别相关。风和热力学的变化分别解释了全球 OHU 的~50%，而南大洋的强迫趋势几乎可以解释所有的全球 OHU。当大气热力学特征保持不变时，这种全球 OHU 是由凉爽的海面温度和感热增量导致的，而当风向固定时，向下的长波辐射占优势。这些结果解决了数十年来海洋-海冰模型模拟在调和 OHU 运输和存储估计方面长期存在的局限性。

ABSTRACT: Since the 1970s, the ocean has absorbed almost all of the additional energy in the Earth system due to greenhouse warming. However, sparse observations limit our knowledge of where ocean heat uptake (OHU) has occurred and where this heat is stored today. Here, we equilibrate a reanalysis-forced ocean sea ice model, using a spin-up that improves on earlier approaches, to investigate recent OHU trends basin-by-basin and associated separately with surface wind trends, thermodynamic properties (temperature, humidity and radiation) or both. Wind and thermodynamic changes each explain ~ 50% of global OHU, while Southern Ocean forcing trends can account for almost all of the global OHU. This OHU is enabled by cool sea surface temperatures and sensible heat gain when atmospheric thermodynamic properties are held fixed, while downward longwave radiation dominates when winds are fixed. These results address long-standing limitations in multidecadal ocean-sea ice model simulations to reconcile estimates of OHU, transport and storage.

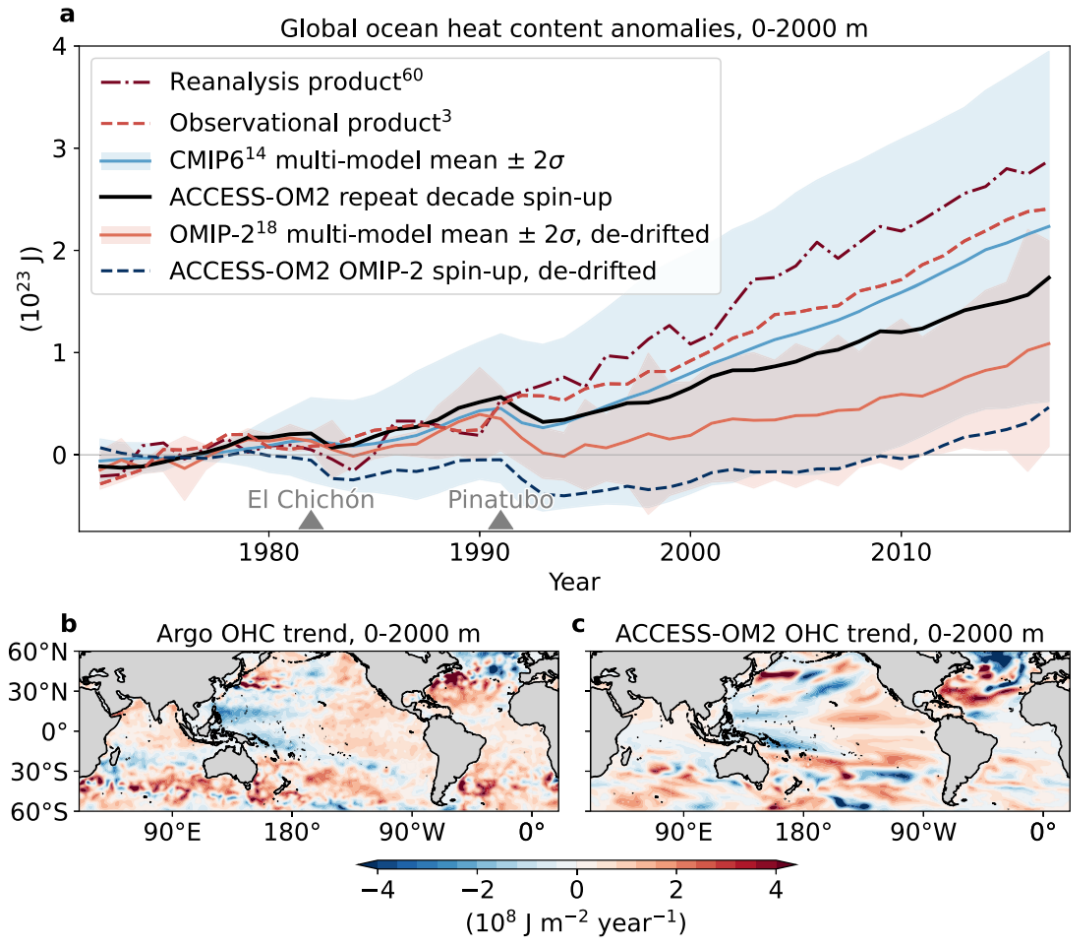

Figure 1. Recent global ocean heat content (OHC) anomalies in observations and hindcast model simulations. **a** Global ocean heat content anomalies (10^{23} J) in the upper 2000 m from ocean reanalysis, observations, 25 fully coupled historical CMIP6 model runs (including their multi-model mean and 2σ variance), the full forcing ocean-sea ice simulation (ACCESS-OM2 repeat decade spin-up, where all atmospheric forcing fields evolve over time), 11 de-drifted OMIP-2 ocean-sea ice model simulations (including their multi-model mean, and 2σ variance) and the de-drifted ACCESS-OM2 OMIP-2-based simulation. For the individual time series of each CMIP6 and OMIP-2 ensemble member, see Supplementary Fig. 2. The two triangle markers highlight the volcanic eruptions of El Chichón in 1982 and Mount Pinatubo in 1991. The baseline period for all time series is 1972–1981. **b, c** Spatial distribution of anomalous upper 2000 m ocean heat content trends over 2006–2017 in the Argo observations and in the full forcing ACCESS-OM2 simulation (10^8 J m^{-2} year^{-1}).

15. 过去 230kyr 亚北极太平洋环境生产力的高纬及低纬强迫

翻译人：刘宇星 11811211@mail.sustech.edu.cn

Liu Y, Zhong Y, Gorbarenko S A, et al. ***High-and low-latitude forcing on the subarctic Pacific environment and productivity over the past 230 kyr****[J]. Marine Geology, 2022, 451: 106875.*

https://doi.org/10.1016/j.margeo.2022.106875

摘要：亚北极太平洋与极地和热带气候有关，是海洋生产力高的区域，对海洋-大气二氧化碳通量很敏感。然而，其生产力动力及模式的驱动机制仍然难以捉摸。利用过去 230 kyr 沉积物岩芯中的生物钡、蛋白石和陆源输入，我们展示了亚北极太平洋的持续高分辨率养分可用性动态，并评估了海冰和北太平洋冰川中水对养分上涌的可能影响在该区域。我们认为，该地区的生产力输出受到与低纬度地区水分和热量相关的淡水输入以及弱阿留申低压下堪察加冰川的冰山融水的控制。这些发现表明，高纬度和低纬度气候系统都迫使高纬度北太平洋海洋环境和初级生产力的演变。

ABSTRACT: The subarctic Pacific Ocean, which is linked to both polar and tropical climates, is an area of high marine productivity and is sensitive to ocean-atmosphere CO2 flux. However, the mechanisms underlying the drivers of its productivity dynamics or patterns remain elusive. Using biogenic barium, opal, and terrigenous input in a sediment core for the past 230 kyr, we present a continuous high-resolution nutrient availability dynamic for the subarctic Pacific Ocean and assess possible changes to sea ice and glacial North Pacific Intermediate Water on nutrient upwelling in the region. We suggest that export production in this region is controlled by the freshwater discharge associated with moisture and heat from low-latitude and the iceberg discharge from Kamchatka glaciations under a weak Aleutian Low. These findings indicate that both high- and low-latitude climate systems forced the evolution of the marine environment and primary productivity in the high-latitude North Pacific.

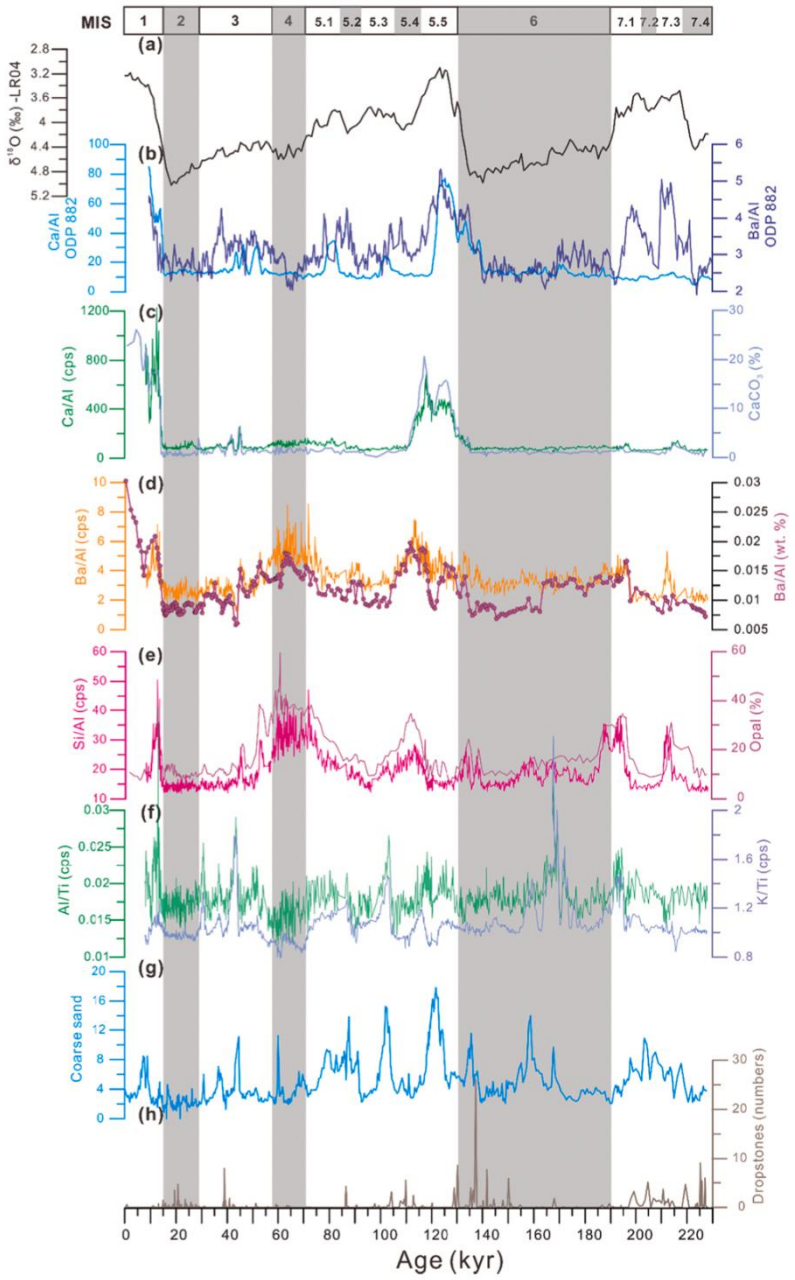

Figure 1. Records reflecting changes in export production and terrigenous supply in core LV63–4-2 over the past 230 kyr in comparison with other records of the study area. (a) $\delta^{18}O$ record of LR04 (Lisiecki and Raymo, 2005); (b) Ca/Al ratio and Ba/Al ratio of ODP site 882 (Jaccard et al., 2009); (c) Ca/Al ratio and $CaCO_3$ content (Yao et al., 2022); (d) Ba/Al ratio (cps) and Ba/Al (wt%) based on geochemical analysis (Yao et al., 2022); (e) Si/Al ratio (cps) and Opal content; (f) Al/Ti ratio (cps) and K/Ti ratio (cps); (g) coarse sand (63–2000 μm) contents and (h) dropstone (>2 mm) contents of core LV63–4-2, respectively.

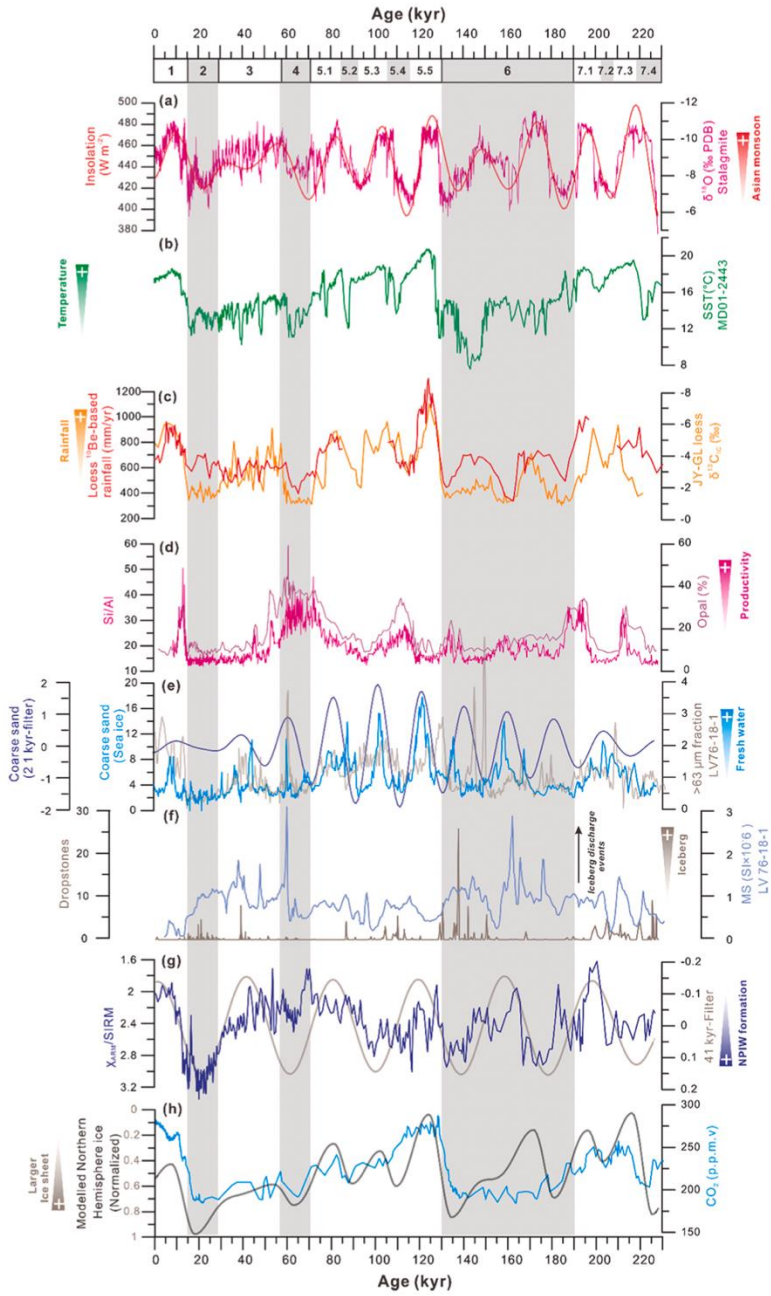

Figure 2. Depth-converted image. Depth-converted mantle reflections, interpreted as the LAB (red) and G-reflection (green). Red dashed line indicates the interpolated depth from 16 Ma to 27 Ma. Best-fitting half-space (solid blue) and plate-cooling (solid black) isotherms are also plotted (1, 53) and have an uncertainty of ±20°C. Results from seismic reflection study across the St. Paul fracture zone are shown by red (top) and green (bottom) stars at 40 Ma and 70 Ma, respectively (13). Dashed gray line with error bars indicates the results from radial anisotropy in the Atlantic Ocean (3). The blue triangles indicate the ensemble of LAB depths observed from previous studies (10) showing widespread LAB depths. Recent results from surface wave tomography (solid dotted blue line) (4) and colocated magnetotelluric experiment (solid dotted brown line) (29) just south of Chain fracture zone have also been plotted. The surface wave tomography and magnetotelluric results have a depth uncertainty of ≥10 to 15 km (4, 29).

16. 理解 8.2 ka 冷事件和当前暖事件期间的全球季风降水变化

翻译人：聂美娟 12232216@mail.sustech.edu.cn

Peng H, Jian L, Bin W, et al. ***Understanding global monsoon precipitation changes during the 8.2 ka event and the current warm period****[J].* *Palaeogeography, Palaeoclimatology, Palaeoecology.585（2022）110757*

https://doi.org/10.1016/j.palaeo.2021.110757

摘要：全球季风降水对水资源、粮食安全和约三分之二世界人口的生计具有深远影响。了解 8.2 ka 冷事件和当前暖事件期间全球季风降水的对比变化有助于更好地理解全球季风降水变化的共同起源及其未来预测。我们分析了一套瞬态气候演变(TraCE-21 ka 模拟)。结果表明，模拟的 8.2 ka 突变降温过程中的季风降水变化与世界范围内的古气候资料具有质的一致性。模拟北半球季风降水显著减少 12.4%，而南半球季风降水增加 4.2%/℃。降温诱导的抑制上升运动在减少北半球降水中起主导作用，水分减少增加了环流效应，而南半球季风降水增强主要是由于水分增加。在 8.2 ka 冷事件中，环流响应加强了北半球季风地区的湿度引起的干旱，导致降水对温度变化过度敏感(12.4%/℃)。相反，在当前温暖期，温室变暖引起的水分和循环效应相互抵消，导致中等灵敏度(1.8%/℃)。尽管融水和温室气体增加导致了截然不同的全球温度变化模式，但全球温度变化受共同的根本原因控制:强烈的北半球-南半球热对比、陆地-海洋热对比和热带海温梯度。湿度的变化对降水量的变化起关键作用，但对空间分布没有影响。我们认为，外部强迫诱导的增温(降温)模式驱动了环流变化(动态效应)，决定了季风降水变化的过去、现在和未来的空间结构。

ABSTRACT: Global monsoon (GM) precipitation has profound impacts on water resources, food security, and the livelihood of about two-thirds of the world's population. Understanding the contrasting changes of GM precipitation (GMP) during the 8.2 ka cold event and the present-day warm event helps better comprehend the common origin of the GMP change and its future projection. We analyzed a suite of transient climate evolutions (TraCE-21 ka simu-lation). We show that the simulated monsoon rainfall changes during the 8.2 ka abrupt cooling event are qualitatively

consistent with the paleoclimate archive collected worldwide. The simulated Northern Hemisphere monsoon (NHM) precipitation significantly decreased by 12.4% per one degree of global mean temperature change (12.4%/°C) while the Southern Hemisphere monsoon (SHM) precipitation increased by 4.2%/°C. The cooling-induced suppressed upward motion plays a dominant role in reducing NHM precipitation, and the reduced moisture adds to the circulation effect, whereas the enhanced SHM precipitation is mainly due to the moisture increase. In the 8.2 ka event, the circulation response reinforces the moisture-induced drought over the NHM region, resulting in an excessive precipitation sensitivity to temperature change (12.4%/°C). In contrast, during the present warm period, the greenhouse warming-induced moisture and circulation effects cancel each other, resulting in a moderate sensitivity (1.8%/°C). Although meltwater and greenhouse gas forcings induce contrasting global temperature change patterns, the GMP changes are governed by common root causes: forced NH-SH thermal contrast, land-ocean thermal contrast, and the tropical SST gradients. The moisture change plays a crucial role in altering precipitation amount but not spatial distribution. We suggest that the external forcing-induced warming (cooling) pattern drives the circulation changes (dynamic effects), determining the spatial structure of the monsoon rainfallchange in the past, present, and future.

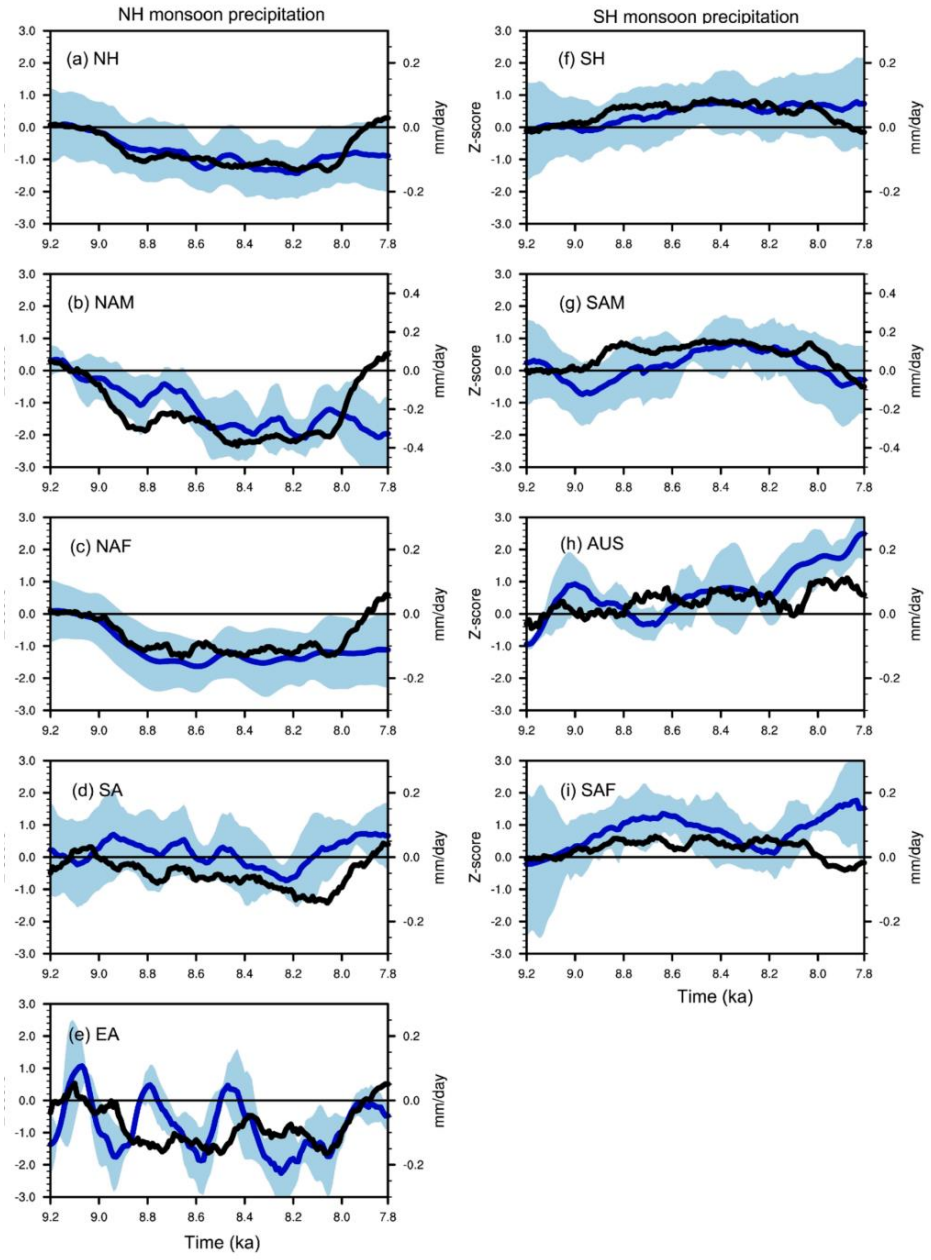

Figure 1. Comparison of the precipitation evolution inferred from the proxy data (blue) and the simulated annual mean precipitation derived from TraCE-AF (black). (a-e) The proxy data averaged over the NH monsoon regions: (a) NH, (b) NAM, (c) NAF, (d) SA, and (e) EA. (f-i) the proxy records averaged over the SH monsoon regions: (f) SH, (g) SAM, (h) AUS, and (i) SAF. The uncertainty of proxy-based precipitation was measured by 1 standard deviation of the spread of the individual proxy record. A 100-yr running mean has been applied to the time series. Z-score denotes the standardized precipitation changes inferred from the proxy data. The simulated annual mean precipitation changes are with reference to the preceding (9.2–9.0 ka) climatology. (For interpretation of the references to colour in this figure legend, the reader is referred to the web version of this article.)

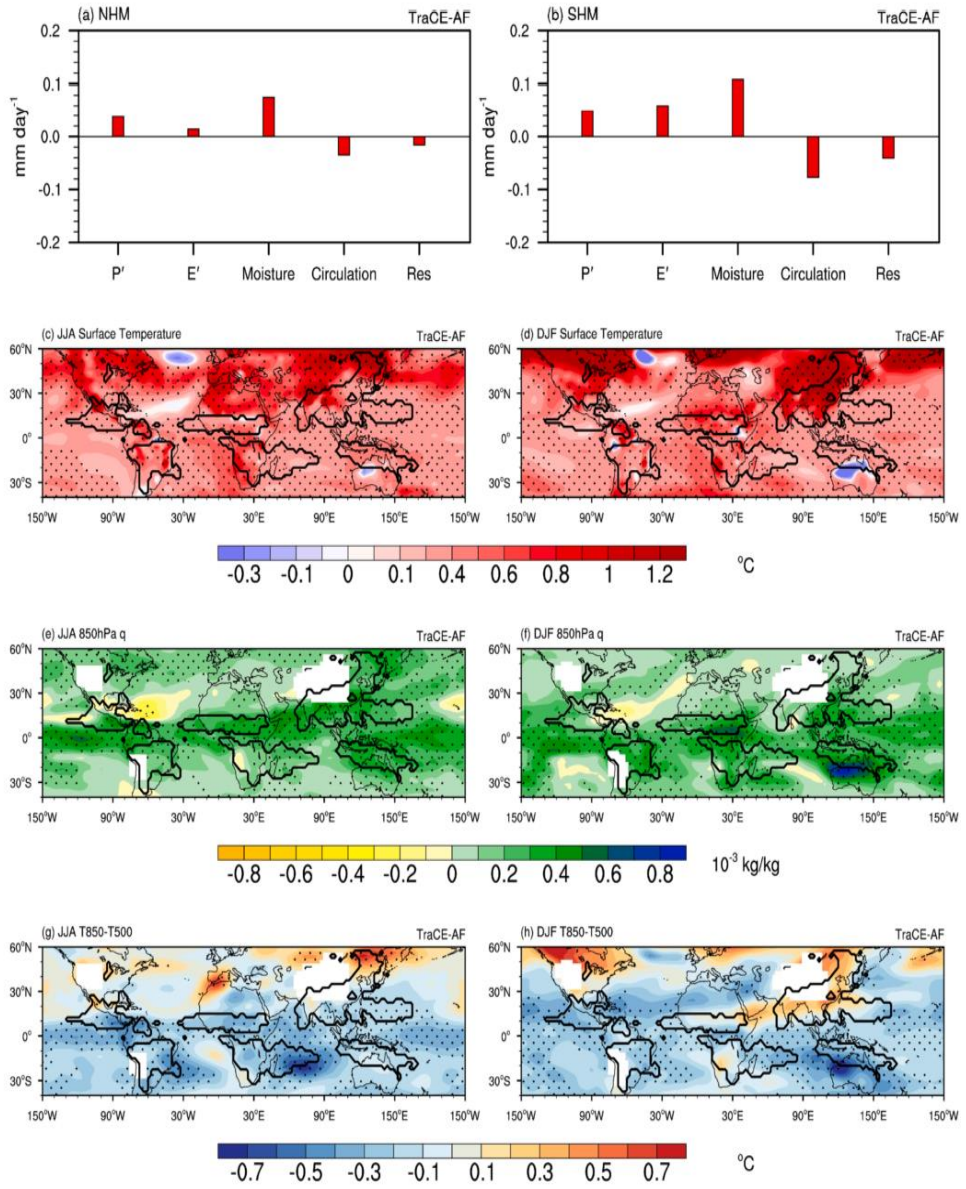

Figure 2. Atmosphere moisture and circulation change during the CWP derived from the TraCE-AF experiment. (a, b) Moisture budget decomposition of local summer precipitation changes. (c) Surface temperature (shadings, ˚C) changes. (e) 850 hPa specific humidity (shadings, kg kg^{-1}) changes. (g) Atmospheric static stability changes (shadings, ˚C) in JJA mean. (c, e, and g) same as (d, f, and h), but for the result in DJF mean. Only the significant regions above the 95% confidence level via a two-tailed Student's *t-test* are dotted.